Non-Arrhenius grain growth in strontium titanate: Quantification of bimodal grain growth

Wolfgang Rheinheimer[1,*], Ephraim Schoof[3], Michael Selzer[2,3], Britta Nestler[2,3] and Michael J. Hoffmann[4]

* Corresponding author, rheinheimer@purdue.edu

1 Purdue University, Materials Engineering, 701 West Stadium Ave, 47907 West Lafayette, Indiana, USA
2 Institute of Digital Materials Science, Karlsruhe University of Applied Sciences, Moltkestr. 30, 76133 Karlsruhe, Germany
3 Institute of Applied Materials, KIT, Strasse am Forum 7, 76131 Karlsruhe, Germany
4 Institute of Applied Materials, KIT, Haid-und-Neu-Str. 7, 76131 Karlsruhe, Germany

Abstract

Strontium titanate is well-known for its non-Arrhenius grain growth, where grain growth coefficients decrease by orders of magnitude between 1350 °C and 1425 °C. This transition is assumed to be caused by the existence and coexistence of two grain boundary types and results in the formation of bimodal microstructures. So far, no quantified data on the transition behavior was available. The present study uses a comparison of experimental microstructures for various heating times and temperatures with simulated microstructures from phase-field simulations considering various fractions of fast-growing grains. The microstructures are compared by means of their grain size distributions. It is found that the fraction of fast-growing grains follows a nucleation-like behavior. Evaluating the present findings with respective literature data, the grain growth transition could be related to a space charge transition where the fast and slow grain boundaries are associated with strong and weak space charge and segregation. Overall, the present study sheds light on general grain growth transitions observed in several perovskite ceramics.

Keywords

Grain growth transition; grain growth; bimodal microstructures; grain size distributions; strontium titanate

1. Introduction

Strontium titanate is well-known for its counterintuitive grain growth behavior between 1350 °C and 1425 °C [1-6]. Grain growth does not follow classical Arrhenius behavior in this temperature range. Instead, grain growth rates decrease by more than one order of magnitude in this temperature range. This grain growth transition was observed using the equation [7]

$$D^2 - D_0^2 = 2\alpha\gamma m \cdot t = kt$$

with the mean grain diameter *D*, the mean grain diameter *D₀* at time *t = 0*, a geometric constant $\alpha \approx 1$, the grain boundary energy γ and the grain boundary mobility m. The grain growth constant $k = 2\alpha\gamma m$ was used to quantify the evolution of the mean grain size ([4], see Fig. 1). A continuously decreasing grain growth rate is evident between 1350 °C and 1425 °C [4]. Below and above this transition regime, thermally activated grain growth occurs [5, 6].

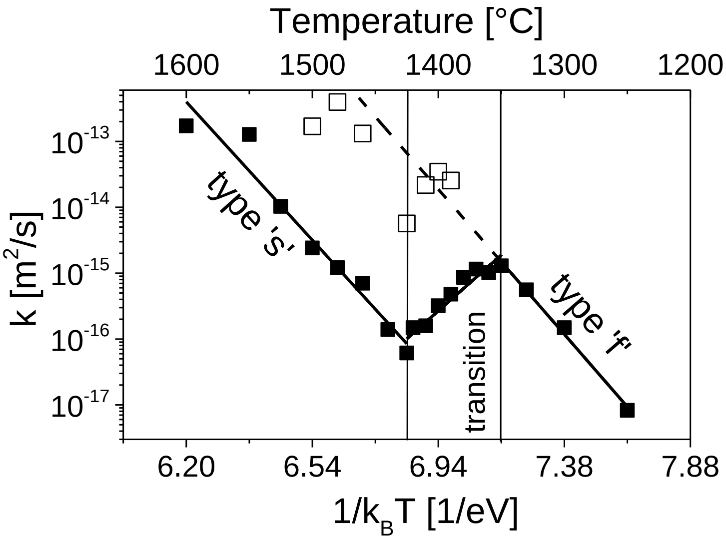

Fig. 1 Arrhenius graph of the grain growth constant of strontium titanate [4, 6].

To date only very few materials are known to show decreasing grain growth rates with increasing temperatures [6]. In the case of strontium titanate and some other perovskites as barium titanate and lithium lanthanum titanate, a close relation to bimodal (or exaggerated) grain growth was reported [5, 6]: with beginning grain growth transition (above 1350 °C), microstructures are bimodal. This is best illustrated by observing microstructures at different temperatures, but after the same heating time. At 1350 °C (lower temperature of the grain growth transition), the microstructure is unimodal (Fig. 2a). With increasing temperature, an increasing fraction of small grains appears in the microstructures (Fig. 2b-d), until at 1425 °C (upper temperature of the grain growth transition) very few large grains are evident (Fig. 2e). These findings resulted in the hypothesis that the grain growth transition is related to a grain boundary transition [4-6] where two different grain boundary types exist [2-4, 8, 9]: a fast low temperature type ('f' in Fig. 1) and a slow high temperature type ('s' in Fig. 1). Accordingly, the grain growth transition indicates a gradual transit of the grain boundary population from the fast type to the slow type with increasing temperature. The coexistence of these two boundary types results in the formation of bimodal microstructures as evident in Fig. 2.

Despite of intense research, the physical difference of the two grain boundary types remains unclear [6]. No structural difference could be observed via TEM [10-12]. Possibly a slight change of the A/B ratio of the perovskite structure ABO_3 occurs at the boundaries [8, 9]. Via the grain boundary grooving technique, it could be shown that the grain boundary energy is lower for the slow high temperature type [3].

However, if microstructures evolve bimodally, the mean grain size and the grain growth constant *k* are not adequate quantities to characterize grain growth. The fraction of fast-growing grains will consume all small grains during grain growth and the evolution of the grain size distribution is no longer self-similar [13]. The self-similarity of microstructural evolution is required in order to apply mean field modeling [13, 14]. This becomes most evident when considering driving forces: mean field modeling assumes driving forces based on mean curvature, e.g. proportional to the inverse mean grain size *1/D* as in Eqn. 1 [14]. The use of a mean grain size does not allow to include the impact of heterogenous grain size distributions. Instead, the driving force for growth of an individual grain depends on the size of its neighbors. Small neighboring grains will result in a large driving force (e.g. Fig. 2e), while an increasing fraction of large neighbors results in a much lower driving force (e.g. Fig. 2b). Note that during bimodal grain growth the driving force can change discontinuously with time, if impingement of large grains occurs. In Hillert's mean field approach, bimodal microstructures were nevertheless considered [13], but without including influences of a local neighborhood. Accordingly, mean field modeling in general and the grain growth constant *k* in particular cannot characterize the grain growth transition of strontium titanate sufficiently.

The scope of the present paper is a quantified description of the grain growth transition and the corresponding evolution of bimodal microstructures in terms of the framework published in the literature [5, 15]. A thorough quantification allows to gain insight on the physical characteristics of the transition, e.g. the nucleation behavior of the two grain boundary types. Since mean field modeling is not adequate, a phase-field simulation was used to model bimodal grain growth. The two grain boundary types were represented with two different grain boundary mobilities. The simulated microstructures were compared to the experiments based on the grain size distributions as the most adequate measure of bimodal microstructures.

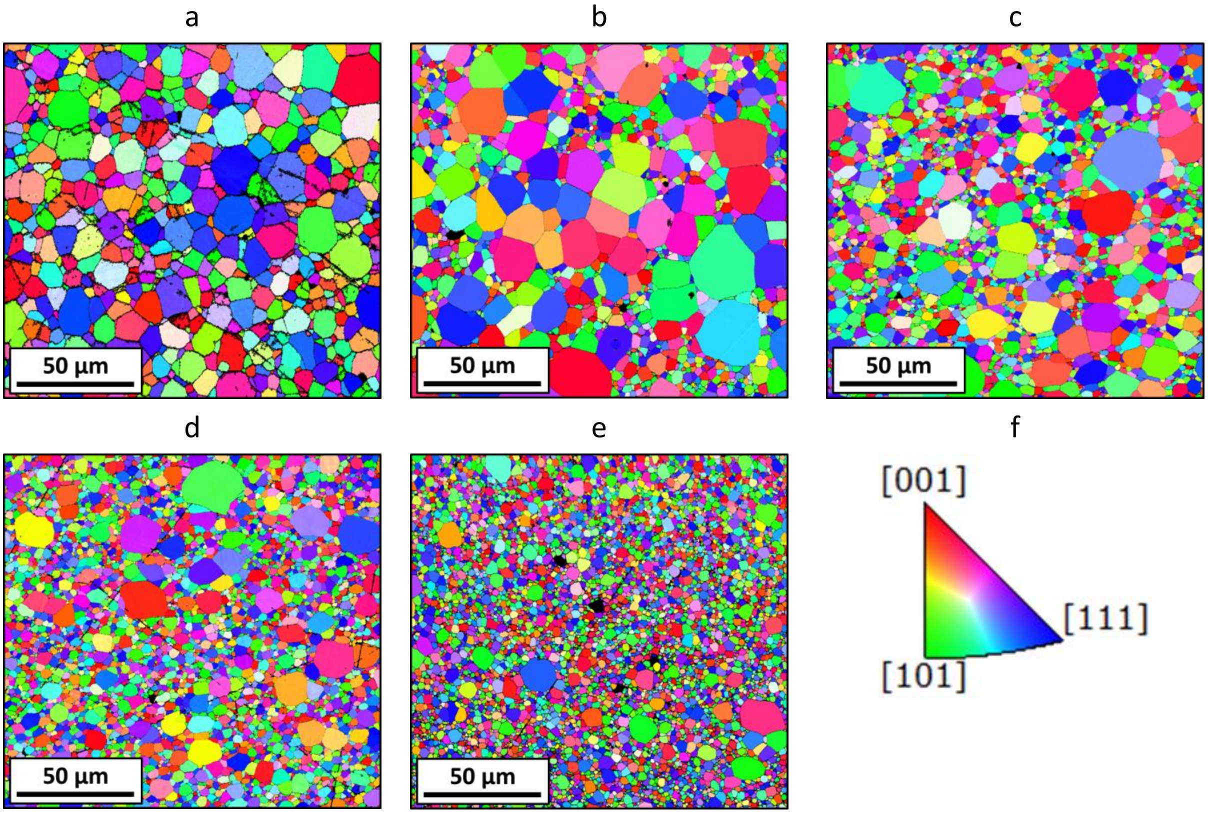

Fig. 2 Microstructures of strontium titanate after 10 h at 1350 °C (a), 1390 °C (b), 1400 °C (c), 1410 °C (d) and 1425 °C (e) as measured by EBSD (orientation colors with respect to the sample surface according to the map in f) [5, 6].

2. Experimental procedure

2.1. Polycrystalline ceramic samples

Stoichiometric ceramic powder was prepared by a mixed oxide/carbonate route based on high purity raw materials ($SrCO_3$ and TiO_2, purity of 99.95 % and 99.995 %, Sigma Aldrich Chemie GmbH, Taufkirchen, Germany). Details of the synthesis are published elsewhere [16-18]. The green bodies were pre-sintered at 1425 °C for 1 h in oxygen to obtain a relative density of 99.5±0.2 % and a uniform grain size distribution with a mean grain size of 1 µm [19].

After pre-sintering, grain growth experiments were done between 1350 °C and 1500 °C in oxygen. For all heat treatments, a tube furnace was used (Carbolite Gero GmbH & Co. KG, Neuhausen, Germany). Heating and cooling rates of 20 K/min and 10 K/min were applied. The heating time was interrupted at specific intervals to observe the microstructure on polished slices.

The microstructures were observed by SEM and EBSD. The typical frame size was 2500 x 2158 pixels (1800 x 1550 to 3000 x 2590) with a step size of typically below 100 nm (75 nm to 170 nm depending on the size of the small grains). The detection rate was typically 98.5 % (min. 96 %). These settings were required to resolve the bimodal microstructures (high resolution to resolve small grains and enough large grains for statistics). The number of grains per measurement was typically 5000 (min. 1000, max. 37000). Edge grains were excluded from the analysis. In some cases, several mappings were used to improve the statistics. To exclude noise in the orientation detection, a minimum grain size of four pixel was used. More details can be found in the supplementary material (**Table S1**).

2.2. Grain growth simulations

2.2.1. Multiphase-field model

In this study, we use a thermodynamically consistent multiphase-field model based on [20]. The basic concept and the necessary equations for the modeling of bimodal grain growth are briefly summarized in the following. For further information on the phase-field approach, the reader is referred to [21-24].

In a system with N grains and of volume V, each grain $\alpha \in \{1,\dots,N\}$ is assigned an order parameter ϕ_α which is part of the N-tuple $\boldsymbol{\phi}(\boldsymbol{x},t) = (\phi_1(\boldsymbol{x},t),\dots,\phi_N(\boldsymbol{x},t))$ and represents the respective volume fraction of the individual grain with a particular crystallographic orientation. The phase fields are dependent on the position $\boldsymbol{x}$ and the time t. Within grain α the order parameter becomes $\phi_\alpha(\boldsymbol{x},t) = 1$ and outside it assumes the value $\phi_\alpha(\boldsymbol{x},t) = 0$. In the transition or diffuse interface region, the value changes smoothly in the range $0 < \phi_\alpha(\boldsymbol{x},t) < 1$. Since ϕ_α represents the volume fraction of the respective grain, the local condition $\sum_\alpha \phi_\alpha(\boldsymbol{x},t) = 1$ must always be fulfilled. The total free energy of the system is expressed as

$$\mathcal{F} = \int_V f(\boldsymbol{\phi}, \boldsymbol{\nabla\phi})\mathrm{d}V = \int_V \varepsilon a(\boldsymbol{\phi}, \boldsymbol{\nabla\phi}) + \frac{1}{\varepsilon}\omega(\boldsymbol{\phi})\mathrm{d}V, \qquad \mathbf{2}$$

with the gradient energy density $\varepsilon a(\boldsymbol{\phi}, \boldsymbol{\nabla\phi})$ and the potential energy density $\omega(\boldsymbol{\phi})/\varepsilon$ representing the contribution of the interfacial energy. The parameter ε is related to the interface width. With the interfacial energy $\gamma_{\alpha\beta}$ at an $\alpha - \beta$ interface, the gradient energy density is calculated as

$$\varepsilon a(\boldsymbol{\phi}, \boldsymbol{\nabla\phi}) = \varepsilon \sum_{\alpha<\beta} \gamma_{\alpha\beta} |\boldsymbol{q}_{\alpha\beta}(\boldsymbol{\phi}, \boldsymbol{\nabla\phi})|^2, \qquad \mathbf{3}$$

where $\boldsymbol{q}_{\alpha\beta}(\boldsymbol{\phi}, \boldsymbol{\nabla\phi}) = \phi_\alpha \boldsymbol{\nabla}\phi_\beta - \phi_\beta \boldsymbol{\nabla}\phi_\alpha$ is the generalized gradient vector normal to the $\alpha - \beta$ interface. The obstacle-type potential energy density

$$\frac{1}{\varepsilon}\omega(\boldsymbol{\phi}) = \frac{16}{\varepsilon\pi^2} \sum_{\alpha<\beta} \gamma_{\alpha\beta}\phi_\alpha\phi_\beta + \frac{1}{\varepsilon} \sum_{\alpha<\beta<\delta} \gamma_{\alpha\beta\delta}\phi_\alpha\phi_\beta\phi_\delta \qquad \mathbf{4}$$

contains a higher order term $\propto \phi_\alpha\phi_\beta\phi_\delta$ to avoid spurious phases at binary interfaces. A detailed discussion of this term can be found in [25]. If $\boldsymbol{\phi}(\boldsymbol{x},t)$ is not in the Gibbs simplex

$$\mathcal{G} = \left\{\boldsymbol{\phi} \in \mathbb{R}^N : \sum_\alpha \phi_\alpha = 1, \phi_\alpha \geq 0\right\}, \qquad \mathbf{5}$$

$\omega(\boldsymbol{\phi}) = \infty$ is set. Based on [26], the evolution equation for each grain α is derived from the energy functional $\mathcal{F}$ by variational derivatives

$$\frac{\partial \phi_\alpha}{\partial t} = -\frac{1}{\varepsilon \tilde{N}} \sum_{\beta \neq \alpha}^{\tilde{N}} M_{\alpha\beta} \left(\frac{\delta \mathcal{F}}{\delta \phi_\alpha} - \frac{\delta \mathcal{F}}{\delta \phi_\beta}\right), \qquad \mathbf{6}$$

where $M_{\alpha\beta}$ is the individual mobility of the $\alpha - \beta$ grain boundary and $\delta\mathcal{F}/\delta\phi_\alpha$ is the variation of the total energy with respect to ϕ_α

$$\frac{\delta\mathcal{F}}{\delta\phi_\alpha} = \frac{\partial f(\boldsymbol{\phi}, \boldsymbol{\nabla\phi})}{\partial\phi_\alpha} - \nabla \cdot \frac{\partial f(\boldsymbol{\phi}, \boldsymbol{\nabla\phi})}{\partial\nabla\phi_\alpha}. \qquad \mathbf{7}$$

The number of locally present phases is given with $\widetilde{N}$.

The simulations are carried out with the Pace3D (Parallel Algorithms for Crystal Evolution in 3D) software package, version 2.1.1 [27]. For each grain, a separate phase-field evolution equation (Eqn. 6) is solved on a finite difference grid with an explicit Euler scheme. We use a Locally-Reduced Order Parameter (LROP) optimization [23, 28] which fixes a maximum number of equations, Eqn. 6, which are solved in each cell of the computational domain. Therefore, the amount of phase-field equations does not rise with increasing total number of grains, because only the locally active phase fields are updated. To reduce simulation time, the two-dimensional domain is decomposed in two directions utilizing the MPI (Message Parsing Interface) standard.

2.2.2. Modeling of bimodal grain growth

We introduce two types of grain boundary mobilities, a slow one M_{slow} and a fast one M_{fast}. They are related by a mobility ratio $L = M_{\mathrm{fast}}/M_{\mathrm{slow}}$., which gives a ratio between the fast and slow mobility. We assume a defined number of grains with a high grain boundary mobility with respect to all other grains. The grain boundaries of the "slow" grains have either a small mobility M_{slow}, when they build a grain boundary together with another slow grain, or a fast one M_{fast}, when they have a grain boundary with a fast grain. In this manuscript, we refer to the number of fast growing grains, since this seems to be practical with respect to the experimental results, where entire grains are counted.

An isotropic interfacial energy $\gamma_{\alpha\beta} = \gamma$ is assumed for all simulations and the higher order therm is scaled with $\gamma_{\alpha\beta\delta} = 10\gamma_{\alpha\beta}$. In order to get a realistic starting configuration for the simulation of bimodal grain growth, we first perform a grain growth simulation with a constant mobility $M_{\alpha\beta} = M$. A domain with $2000\Delta x \times 2000\Delta y$ is filled with 20000 grains using a voronoi tessellation algorithm. Periodic boundary conditions are applied. Eqn. 6 is solved numerically for each grain until 10000 grains remain. The resulting microstructure has a unimodal grain size distribution.

For the present study, we simulated microstructure evolution with mobility ratios $L = M_{\mathrm{fast}}/M_{\mathrm{slow}}$ of 10, 15, 20, 30 and 50. The fraction of fast growing grains N_{f} (number of fast grains divided by 10000) evaluated for each L was 0, 0.005, 0.025, 0.05, 0.08, 0.11, 0.13, 0.16, 0.19, 0.23, 0.26, 0.29 and 0.5. For evaluation reasons, a timescale is given for each frame of the simulated microstructure. However, since an arbitrary mobility M_{slow} was chosen, the time only serves the purpose of comparability and has no further physical meaning.

2.3. **Comparison of experimental and simulated grain size distributions**

The present study bases on a comparison of simulated and measured grain size distributions. The comparison of measured and simulated distributions is a complex problem, since a bimodal microstructure evolution has many parameters (mobility ratio L, fraction of fast grains N_f and simulation time t). A sketchy view on the simulation results suggests that the same simulated grain size distribution can be achieved with a high L and a low N_f as well as a low L and a high N_f. However, this is not the case, as the following discussion underlines. Here, we ignore local neighborhood of large and small grains. The discussion will be slightly different as soon as the large grains show significant impingement. By setting N_f, we define the number of fast-growing grains. While statistically, some of them are going to shrink, a fraction is going to grow and move to the tail of the grain size distribution. Their number can be assumed to be only influenced by N_f, if the initial microstructure is kept constant. Accordingly, N_f dictates the absolute number of grains in the tail of the grain size distribution. A second maximum will eventually form in the grain size distributions.

The mobility ratio L is scaling how quickly the fast grains are moving to the tail of the grain size distributions: if L is close to one, it takes a long time until the fast grains also become large grains. During this time, the small grain population also grew so that a significant number of small grains is lost. As such, the relative fraction of large grains in the tail of the grain size distribution increases. At the same time, the peak of small grain population shifted to larger grain sizes. For a higher L, less time is required for the fast grains to reach the tail of the grain size distribution. In this time, fewer small grains are lost due to grain growth and less grain growth occurred in the small grain population.

This argumentation only holds for a dilute population of large grains. For significant impingement between large grains, the relationship is more complex. The height and position of both maxima and, more general, the shape of the grain size distribution depends on L and N_f. As a result, the grain size distributions are distinguishable for each set of L and N_f for all times.

For a proper representation of large grains, all distributions show area fractions. The simulated grain size distributions were normalized to their mean grain size using area fractions as obtained by area weighting. However, the mean grain size of the measured grain size distributions strongly depends on the statistical representation of the large grains. As such, normalizing the measured distributions to their mean grain size was not an adequate way to comparing them with the simulated grain size distributions. Thus, we used the shape and peak of the small grain fraction to scale the measured grain size distributions to the simulated ones.

The grain growth simulations resulted in a collection of microstructures and corresponding grain size distributions for various N_f, L and simulation times t. In this study, only the grain size distributions were used to match simulated and experimental data. The mobility ratio of $L = 50$ yielded the best agreement between simulated and experimental microstructures. A discussion on the experimental evidence for this number follows in section 3.2. For each experimental dataset with multiple heating times, we compared the experimental grain size distributions with those obtained for various N_f and t from simulations and identified the closest match as shown exemplary in Fig. 3, Fig. 4 and Fig. 5. Additional datasets are contained in the supplementary material.

3. Results and discussion

3.1. Microstructure evolution

The experimental microstructure evolution at 1360 °C is shown in Fig. 3 after 1 h (a), 5 h (b) and 10 h (c). A color map for the orientation measured by EBSD is shown in Fig. S1 a. Very pronounced bimodal grain growth is evident. After 2 h, the large grain population is still diluted. After 10 h, significant impingement occurred. Fig. 3 d-f shows the simulated microstructures using an initial fraction N_f of fast grains of 0.29 after simulation times $t = 10$, 14 and 16 in d, e and f, respectively. In general, the microstructural appearance is very similar. However, the similarity between experiments and simulations is more evident if the grain size distributions are compared. In Fig. 3 g-i, both distributions show a very similar shape. Thus, it can be concluded that the simulated microstructures accord well with the measured ones.

Analogue to Fig. 3, the microstructure evolution at 1390 °C is illustrated in Fig. 4 after 2 h (a), 5 h (b) and 10 h (c) along with the simulated microstructures (d-f) and the comparison of the corresponding grain size distributions (g-i). The measured microstructures still perform bimodal grain growth, but compared to 1390 °C (Fig. 3), the fraction of large grains is lower. Accordingly, initially $N_f = 0.19$ of fast grains were needed in the simulation to obtain comparable microstructures (Fig. 4 d-f) and good agreement in the grain size distributions (Fig. 4 g-i).

As third example, the microstructure evolution at 1480 °C is displayed in Fig. 5 after 0.1 h (a), 0.2 h (b), 0.5 h (c), 1 h (d) and 2 h (e). Very pronounced bimodal grain growth is apparent. Impingement of large grains starts after 0.5 h (c) and is very significant after 2 h (e). Very similar microstructures are obtained in the simulation with initially $N_f = 0.05$ fast growing grains (Fig. 5 f-j). The grain size distributions are very similar as well, although significant noise appears in the measured distributions for longer heating times. This is attributed to weaker statistics for the large grain population.

For other temperatures, a comparison of simulated and measured microstructures and grain size distribution analogue to Fig. 3, 4 and 5 can be found in the supplementary material further providing initial fractions of fast grains needed to match experimental and simulated microstructures for other temperatures.

Besides the generally good agreement between measured and simulated grain size distributions, there are two minor differences. First, the shape of the first maximum (i.e. the small grain population) does not match perfectly in some cases. The measured curves are steeper on the left side compared to the simulations (and less steep on the right side).

Second, the shape of the second maximum (i.e. the large grain population) is in general somewhat narrower in the simulations compared to the experiment.

These differences trace back to various sources. The simulations were done in 2D, while the experiments involve 3D. The dimensionality is known to have an impact on the grain morphology [29] and might also contributes to the grain size distribution. In addition, the resolution of the EBSD measurements plays a role for the shape of the grain size distributions at small grain sizes: the pixel size of ~100 nm along with the need of four pixels for a grain results in some data loss for small grains. Finally, the statistics for large grains tend to be poor as their total number counted in EBSD is low compared to the small grains. This becomes obvious at temperatures above 1460 °C for longer heating times as detailed in the supplementary material. As such, the reported match between experiments and simulations is somewhat uncertain for some cases. For 1460 °C after 10 h and 20 h and 1500 °C after 3.5 h, no match could be found at all. More discussion on the methods and possible sources of uncertainty are discussed in section 3.3.

Nevertheless, the overall agreement in simulation and theory is still convincing. Accordingly, it seems to be justified to use the initial fractions of fast grains as obtained by the simulation for further discussion.

Based on the presented findings, the microstructure evolution of strontium titanate can be summarized as follows:

- Below 1350 °C, unimodal microstructures were found. Their mobility is attributed to the low temperature Arrhenius line (type 1 in Fig. 1).
- From 1350 °C on, a fraction of small grains appears in the microstructures. Their mobility seems to be attributed to the high temperature Arrhenius line (type 2 in Fig. 1). The fast grains still seem to follow type 1 growth.
- This fraction increases with increasing temperature but does not reach one at the upper temperature of the grain growth transition (1425 °C).
- The assumption of an initially pre-defined fraction of fast grains is confirmed. The number density of fast grains does not change during growth.
- The ratio of fast and slow growing grains changes with time only due to bimodal grain growth.
- Above 1425 °C, the fraction of fast grains is small. Due to the fast grain growth, bimodal microstructures with impingement of the large grains are evident.

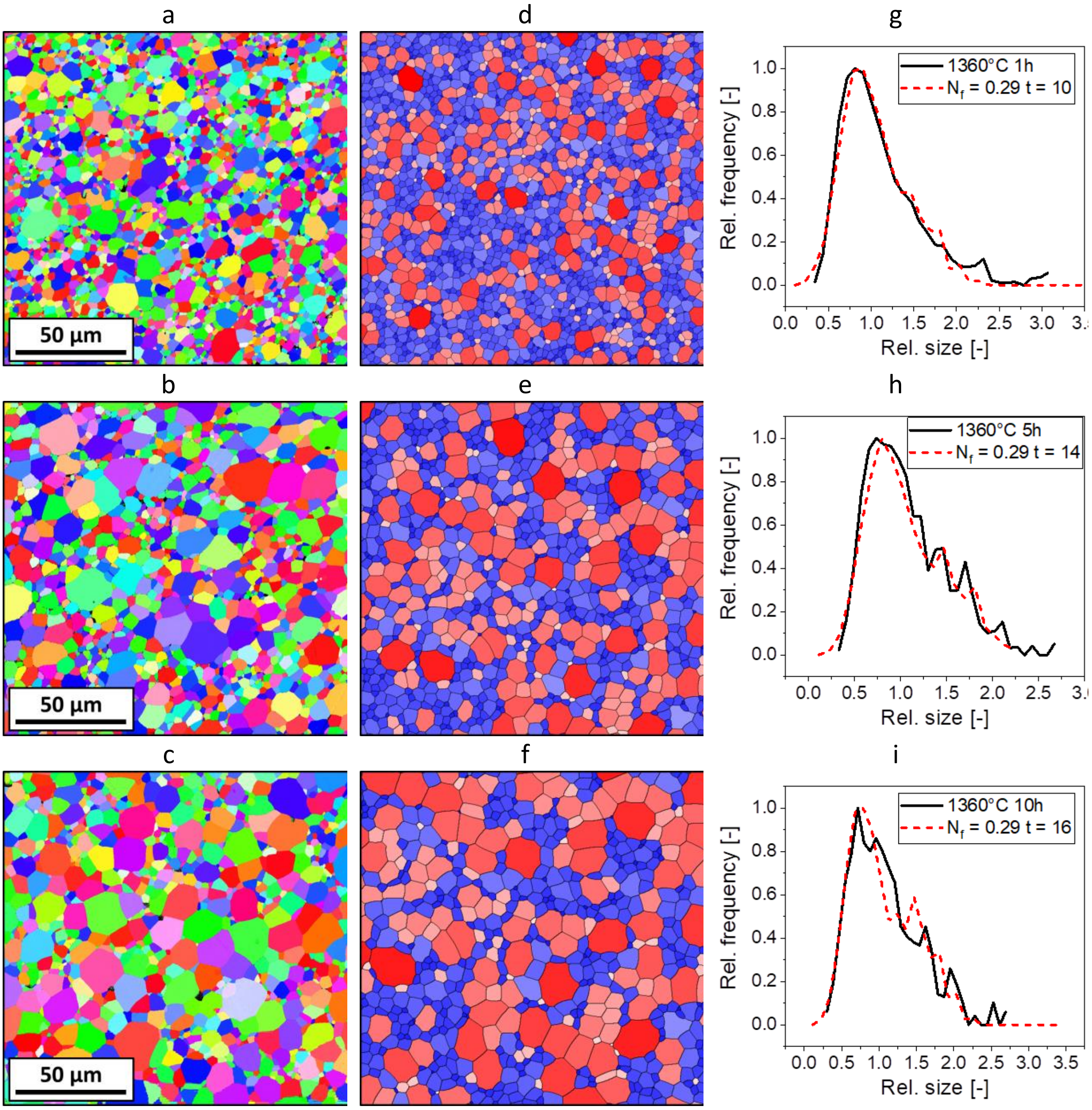

Fig. 3 Microstructure evolution at 1360 °C. EBSD images of the microstructures after 1 h (a), 5 h (b) and 10 h (c). d-f simulated microstructures corresponding to a-c. g-h comparison of measured and simulated grain size distribution. The color in a-c represent the surface orientation of the grains according to the legend in Fig. S1 a. In d-f, the color refers to the type of the respective grain (blue: slow, red: fast). The saturation illustrates the individual grain size according to the legends in Fig. S1 b and c.

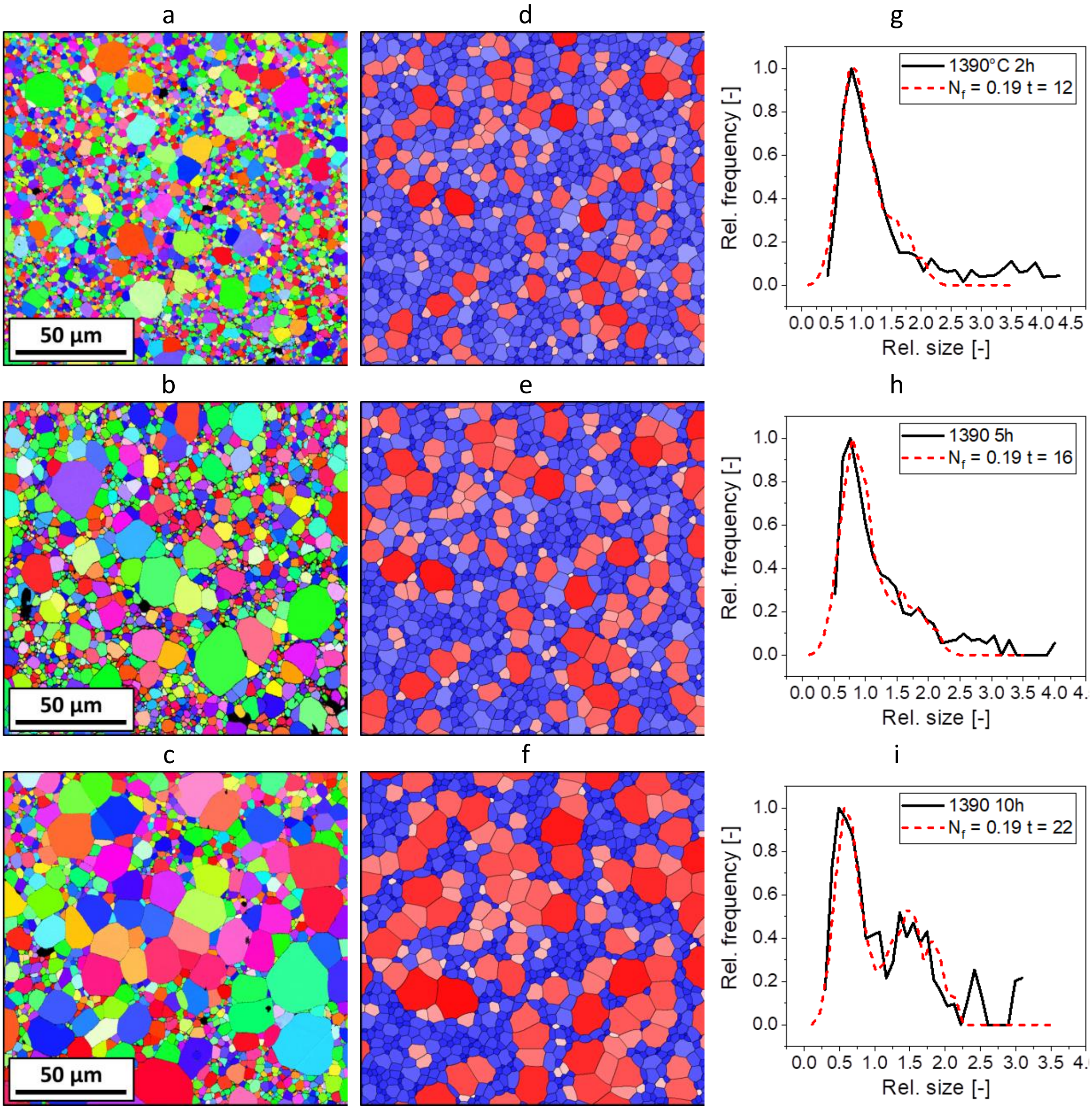

Fig. 4 Microstructure evolution at 1390 °C. EBSD images of the microstructures after 2 h (a), 5 h (b) and 10 h (c). d-f simulated microstructures corresponding to a-c. g-i comparison of measured and simulated grain size distributions.

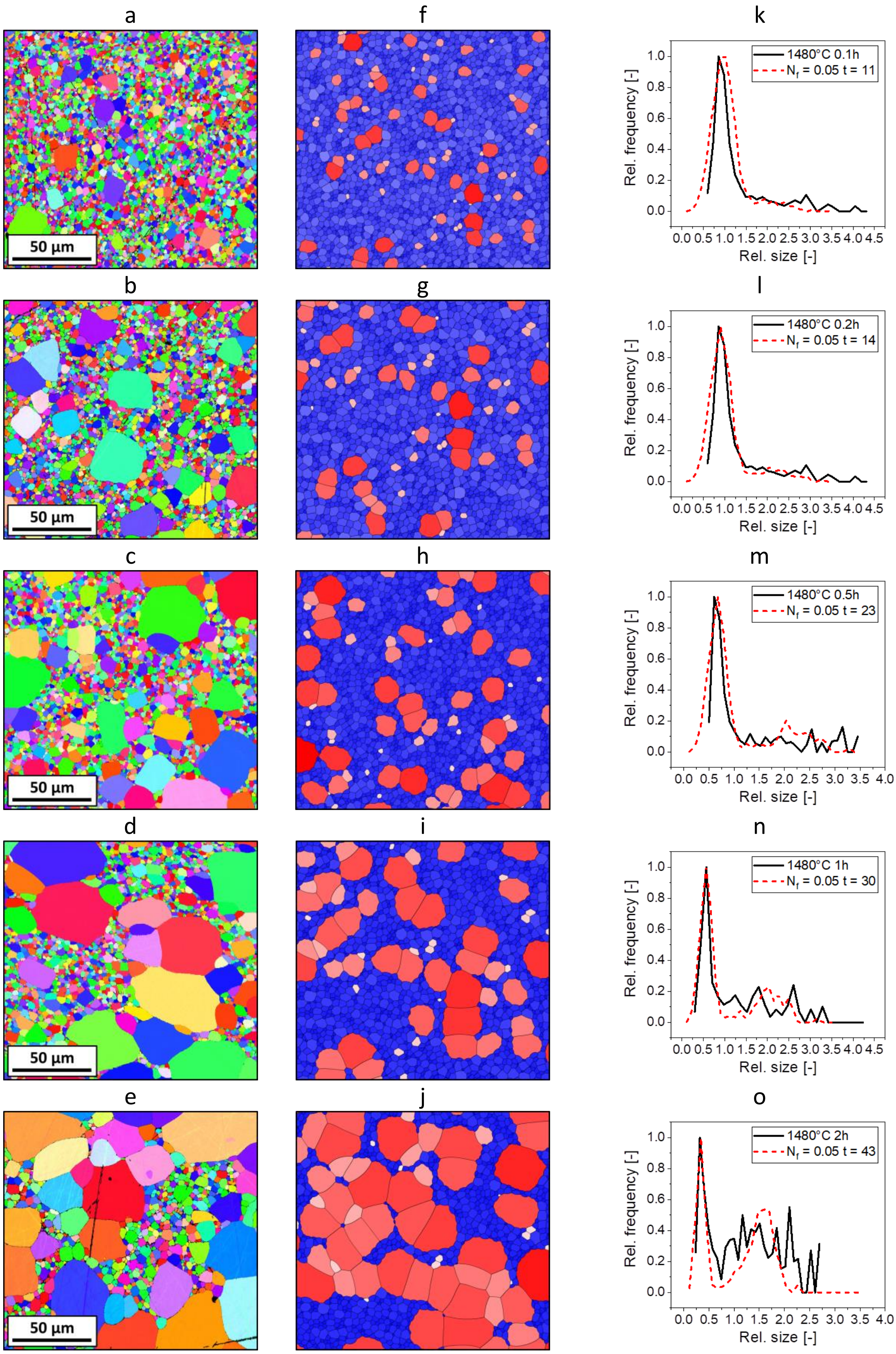

Fig. 5 Microstructure evolution at 1480 °C. EBSD images of the microstructures after 0.1 h (a), 0.2 h (b), 0.5 h (c), 1 h (d) and 2 h (e). f-j simulated microstructures corresponding to a-e. k-o comparison of measured and simulated grain size distributions.

3.2. Transition behavior and its interpretation

The initial fractions N_f of fast grains used for the simulation are shown in Fig. 6 in an Arrhenius graph along with the grain growth constant from Fig. 1. The scale of N_f is logarithmic. At 1350 °C microstructures were observed to be unimodal for all observed heating times (see supplementary material). Thus, N_f was assumed to be one. Possibly the grain size distributions were initially bimodal, but this state was missed by the first observation of microstructure because of impingement of the large grains. In this case N_f is lower than one.

Fig. 6 shows that N_f decreases with increasing temperature. This decrease starts with the grain growth transition itself at 1350 °C. However, it does not end with the grain growth transition (1425 °C); the small fraction of large grains still causes very strong bimodal grain growth with impingement of large grains at higher temperatures. This general behavior accords well with previous findings [4, 5]. Fig. 6 also shows that the decrease of N_f is exponential resulting in a line with negative slope in the Arrhenius graph. Accordingly, N_f can be expressed by the equation

$$N_\mathrm{f}(T) = C \ \cdot e^{-\frac{\Delta G}{k_\mathrm{B} \cdot T}} \qquad \mathbf{8}$$

with a change in free energy ΔG and a constant C. In this form, N_f seems to follow classical nucleation theory. However, according to the negative slope, ΔG is negative and, thus, is not related to a nucleation barrier or an activation energy. Nevertheless, we can summarize that the grain boundary transition seems to follow a nucleation-like behavior, although it is not clear which physical process this nucleation refers to.

While the present paper does not aim on clarifying the atomistic mechanism of the grain growth transition of strontium titanate but only to quantify the microstructure evolution during the transition, the provided information can be discussed in terms of existing ideas. It was argued recently that the grain boundary transition involves a change in grain boundary energy [3]. Following this study, the transition of an individual boundary depends on its grain boundary energy. As the grain boundary energy is anisotropic and, as such, spans over some range for the grain boundary population of a polycrystal, it is likely that the grain boundary transition occurs at different temperatures for different boundaries [3]. In this regard, the thermally activated appearance in Eqn. 8 refers to the thermal activation of this grain boundary transition while more and more individual boundary planes transit to the slow type in a nucleation-like way.

From an atomistic perspective, grain growth in strontium titanate proceeds by disconnection motion [10-12]. A disconnection refers to an atomistic step associated with a grain boundary dislocation component. Despite of intense research, the cited studies could not find a difference in the properties of the disconnection for fast low-temperature and slow high-temperature type. For both cases, the orientations of the step planes are mostly assigned to {100} and {110}. According to the authors, the atomistic mechanism of grain boundary motion does not change between the two different grain boundary types. This agrees well with the slope of the Arrhenius plot in Fig. 6, as both the low and high temperature part have almost the same slope and the same activation energy of about 7.5 eV.

The present results indicate that the grain growth transition does not change the atomistic mechanism of grain boundary motion but impacts the grain boundary energy. One possible mechanism that fulfills both criteria is a transition of the space charge and segregation as discussed before [6, 19, 30-32]. In this framework, the slow and fast types refer to grain boundaries with and without space charge and segregation of charged defects. Segregating defects can be intrinsic as e.g. metal vacancies, but also extrinsic as impurities [31-34]. Following an approach similar to solute drag [35], boundaries with space charge require the segregated point defects to diffuse along with the boundaries resulting in a dragging effect. In contrast, a boundary without (or with less) space charge can move with no (or at least less) diffusional drag yielding a higher grain boundary mobility. It should be noted that the equilibrium state of a grain boundary in strontium titanate does involve space charge for all temperatures investigated in this study [31, 33, 34, 36]. The grain boundary state without space charge refers to non-equilibrium and is associated with a higher grain boundary energy [37-39]. This hypothesis agrees well with findings by Kelly at al., where a lower grain boundary energy was found for the slow high temperature type as discussed above [3]. In addition, a TEM-EDS analysis has shown accumulation of strontium vacancies for small grains, but not for large grains [8, 9]. Accordingly, there is evidence for the grain boundary type to be related to space charge and segregation. However, fully understanding the mechanism requires a more detailed investigation of diffusion kinetics and thermodynamics of space charge along with a careful TEM investigation of the grain boundary chemistry and defect chemistry in forthcoming research [6, 17, 18, 31].

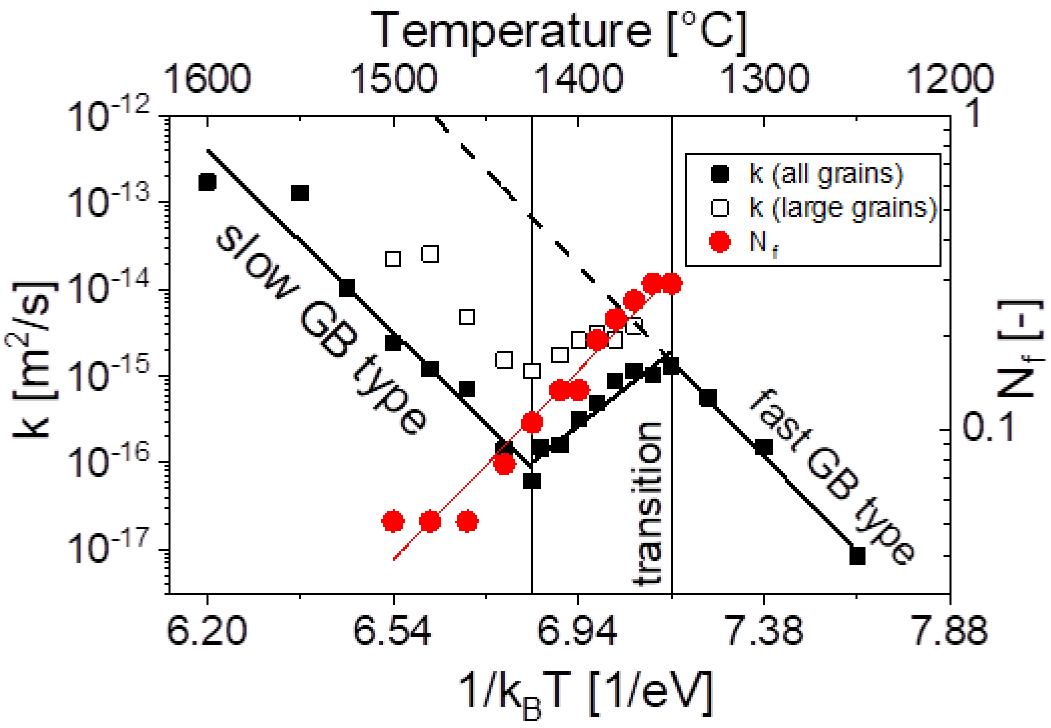

Fig. 6 Temperature dependent fraction of fast grains N_f along with the grain growth constant *k* of large and small grains. For the grain growth coefficient of large grains, a different approach based on Eqn. 9 was used compared to Fig. 1. A detailed description can be found in section 3.3

3.3. Some remarks on the methods used in this study

The focus of this paper is a quantification of the grain growth transition of strontium titanate based on microstructure characterization. We used a simplified approach which cannot give absolute numbers on the scale of individual boundaries; the numbers of fast grains are on the scale of entire grains. In this regard, some general discussion on the chosen approach is appropriate.

The transition of boundaries is usually believed to be correlated to the grain boundary energy [40-43]. In general, grain boundaries should be considered on an individual scale: the properties (i.e. energy or mobility) of each boundary depend on lattice misorientation and grain boundary plane inclination [44]. Thus, the assumptions for the present simulations simplify the real parameter set as entire grains were assumed to grow fast, while this property should be considered on the scale of individual grain boundary planes [5]. Several studies report on the impact of the distribution of individual grain boundary planes with different mobility on the overall microstructure evolution [8, 45-47]. Recently it was found that bimodal microstructures only arise from a mix of two different grain boundary populations with different mobility, if the grain boundary planes tend to be neighboring and, thus, several fast grain boundary planes adjoin at a single grain [48]. It was beyond the scope of this study to re-enact such a simulation. We do not have information on the spatial distribution and transition on the scale of GB planes from experiment. Our focus was to reconstruct the fraction of entire grains. Accordingly, we do not claim that the fractions in Fig. 6 apply on grain boundary planes, but only on entire grains. A more detailed computational study with locally resolved grain boundary properties can be the scope of a forthcoming investigation as the simulation framework Pace3D is capable to account for this information.

Another issue is the mobility ratio between the fast and slow grain population. A comparison of simulations with mobility ratios of 10, 15, 20, 30 and 50 with the experimental microstructure evolution resulted in best agreement for a ratio of 50. In Fig. 1 the difference between the two Arrhenius lines is about two orders of magnitude (50-330 depending on *T*). In this regard, it must be pointed out that for bimodal microstructure evolution the grain growth constant k obtained by the mean grain size of only large grains cannot reflect the behavior of individual grains. By using the approach from Eqn. 1 on a large grain, it is assumed that the neighborhood of the large grain is of a similar size. As driving force for grain growth is assumed to be curvature, a very low driving force is assumed by this approach yielding unnaturally high mobility coefficients if the true neighborhood consisted of smaller grains. Accordingly, in a bimodal microstructure, this assumption does not hold and yields too high growth coefficients. A more appropriate approach would be to interpret large grains as single crystals growing into a more fine-grained matrix. This approach assumes the driving force for the large grains to be given by the curvature of small neighbors and yields the growth equation [19]:

$$D_{\mathrm{large}}(t) = 6 \cdot \frac{k_{\mathrm{fast}}}{k_{\mathrm{slow}}} \left[\sqrt{k_{\mathrm{slow}} t + D_{\mathrm{small},0}^2} - D_{\mathrm{small},0} \right] + D_{\mathrm{large},0} \qquad \mathbf{9}$$

Here, the mean size of the large and small grains are D_{large} and D_{small}, respectively. A subscript of 0 refers to the time $t = 0$. The grain growth coefficients of large and small grains are k_{fast} and k_{slow}. Eqn. 9 was fitted to the data reported in the literature [4, 6]. The obtained growth coefficient for large grains are plotted in Fig. 6 and are much lower than in Fig. 1. The difference between fast and slow grain growth coefficients in Fig. 6 is between 3 and 20, which is much less than 50 – 330. However, Eqn. 9 assumes only small neighbors for large grains. As soon as significant impingement occurs, this assumption does not hold, and true driving forces will be lower than assumed. In this case Eqn. 9 yields too low growth constants for the large grains and, thus, represents a minimum estimate. Accordingly, we now have a maximum (50 - 330) and minimum estimate (3 - 20) for the ratio of fast to slow growth coefficient. From this perspective, focusing on mobility ratios of 10 – 50 and selecting 50 for the presented grain growth simulations seems to be reasonable.

The current simulations only investigated the effect of the grain boundary mobility. The grain boundary energy was kept constant and isotropic. Indeed, the grain boundary energy is anisotropic for $SrTiO_3$ [15]. If the anisotropy of the grain boundary energy changes, the local morphology (i.e. dihedral angles at triple lines) changes. As a result, the curvature of individual boundary planes and, thus, their driving forces change. While little experimental information on this effect is available yet, some simulations treated this problem yielding no conclusive trend [47, 49, 50]. The present simulations did not include this effect. However, the good agreement in the grain size distributions validates that the employed approach is acceptable as long as the morphology itself is not considered. Note that recent results indeed indicated a change of the grain boundary energy associated with the grain boundary transition [3].Moreover, the grain boundary mobility of strontium titanate is known to be anisotropic as well [19]. The spread in mobility was found to be in the order of a factor of two. It is obvious that under these conditions the experimental grain size distributions must be broader than the simulated ones. More specifically, the large grain population, since those grains have a longer growth history and, thus, had more opportunity to differ from each other while the small grain population did not grow much at all. As the simulations do not consider anisotropic grain boundary properties, some mismatch is to be expected.

Finally, it should be pointed out that in the simulations the fraction of fast grains was defined initially, and we used the assumption 'once fast, always fast' for the grain boundaries. Despite this strong assumption, the real and virtual grain size distributions match well. Accordingly, in the grain growth transition of strontium titanate, the fraction of fast grains depends only on temperature, not on time. This is in contrast to the transition behavior of other materials as e.g. yttria [51, 52] and spinel [53]. If a time dependent transition exists, a transition of fast grain boundaries (i.e. the low temperature type) to slow grain boundaries is expected.

4. Summary and conclusions

Strontium titanate shows a remarkable grain growth transition where the grain growth coefficient decreases by orders of magnitude between 1350 °C and 1425 °C. This transition was found to be coupled with bimodal microstructures. In a previous study, the grain growth transition was reported to involve a decreasing fraction of large grains with increasing temperature. This resulted in a simple grain growth model that based on the existence of two grain boundary types. These types were assumed to be stable at different temperatures. In this case the grain growth transition resembles the transition of the grain boundary type with temperature. However, no quantitative data on this grain boundary transition behavior were available so far. The present analysis presents quantified data for this grain boundary transition and provides new insight into the physics of this transition. For the quantification, a large dataset of experimental microstructures for different heating times and temperatures was compared with simulated microstructures. The phase-field grain growth simulations considered two different grain populations with different grain boundary mobilities. The initial fraction of fast grains and the mobility ratio were changed. Simulated and experimental microstructures were compared by means of grain size distributions. Good agreement between experiments and simulations was found for all microstructures where the statistics of both grain populations are sufficient. As a result, a nucleation-like behavior of the grain growth transition was found, as the fraction of large grains follows a classical nucleation equation.

Overall, the present results along with published information propose that the grain growth transition is caused by a grain boundary transition that does not change the atomistic mechanism of grain boundary motion but impacts the grain boundary energy. This might refer to a space charge and segregation with the slow and fast boundaries being those with and without space charge. TEM-EDS measurements from the literature provide evidence for this assumption. Considering a diffusional drag mechanism as solute drag, the difference in mobility stems from a different amount of diffusion of segregated point defects needed for grain boundary motion. The change in grain boundary energy for the two grain boundary types might refer to the different amount of segregation.

The transition itself might reflect the anisotropy of the grain boundary energy: the difference in grain boundary energy and segregation between both grain boundary types would result in different transition temperatures and yield a gradual transformation of the fast low-temperature type to the slow high-temperature type with increasing temperature. More research is needed to detail the mechanism, particularly regarding diffusion kinetics and thermodynamics of space charge and a complementing careful chemistry investigation of the grain boundary chemistry.

Acknowledgements

We thank Daniel Schneider for fruitful discussions. This work was partially supported by the German-Israel Fund (GIF) under Grant No. I-1276-401.10/2014, by the Deutsche Forschungsgemeinschaft (DFG) within the SPP 1959 under Grant No. HO 1165/20-1 and by the 'VirtMat' initiative of the Helmholtz programme oriented research.

References

[1] L. Amaral, M. Fernandes, I. M. Reaney, M. P. Harmer, A. M. R. Senos, and P. M. Vilarinho, "Grain growth anomaly and dielectric response in ti-rich strontium titanate ceramics," *The Journal of Physical Chemistry*, vol. 117, pp. 24787–24795, 2013.

[2] M. Bäurer, D. Weygand, P. Gumbsch, and M. J. Hoffmann, "Grain growth anomaly in strontium titanate," *Scripta Materialia*, vol. 61, no. 6, p. 584–587, 2009.

[3] M. N. Kelly, W. Rheinheimer, M. J. Hoffmann, and G. S. Rohrer, "Anti-thermal grain growth in srtio3: Coupled reduction of the grain boundary energy and grain growth rate constant," *Acta Materialia*, vol. 149, pp. 11–18, 2018.

[4] W. Rheinheimer and M. J. Hoffmann, "Non-arrhenius behavior of grain growth in strontium titanate: New evidence for a structural transition of grain boundaries," *Scripta Materialia*, vol. 101, pp. 68–71, May 2015.

[5] W. Rheinheimer and M. Hoffmann, "Grain growth transitions of perovskite ceramics and their relationship to abnormal grain growth and bimodal microstructures," *Journal of Materials Science*, vol. HTC 2015, pp. 1–10, 2015.

[6] W. Rheinheimer and M. J. Hoffmann, “Grain growth in perovskites: What is the impact of boundary transitions?,” *Current Opinion in Solid State and Materials Science*, vol. 20, no. 5, pp. 286 – 298, 2016.

[7] W. Burton, N. Cabrera, and F. Frank, “The growth of crystals and the equilibrium structure of their surfaces,” *Philosophical Transactions of the Royal Society of London Series A-Mathematical and Physical Sciences*, vol. 243, no. 866, pp. 299–358, 1951.

[8] M. Bäurer, S.-J. Shih, C. Bishop, M. P. Harmer, D. Cockayne, and M. J. Hoffmann, “Abnormal grain growth in undoped strontium and barium titanate,” *Acta Materialia*, vol. 58, pp. 290–300, 2010.

[9] S.-J. Shih, S. Lozano-Perez, and D. J. H. Cockayne, “Investigation of grain boundaries for abnormal grain growth in polycrystalline srtio3,” *Journal of Materials Research*, vol. 25, no. 2, pp. 260–265, 2010.

[10] H. Sternlicht, W. Rheinheimer, M. J. Hoffmann, and W. D. Kaplan, “The mechanism of grain boundary motion in srtio3,” *Journal of Materials Science*, vol. 51, pp. 467–475, 2015.

[11] H. Sternlicht, W. Rheinheimer, R. E. Dunin-Borkowski, M. J. Hoffmann, and W. D. Kaplan, “Characterization of grain boundary disconnections in srtio3 part i: the dislocation component of grain boundary disconnections,” *Journal of Materials Science*, vol. 54, pp. 3694–3709, Mar 2019.

[12] H. Sternlicht, W. Rheinheimer, J. Kim, E. Liberti, A. I. Kirkland, M. J. Hoffmann, and W. D. Kaplan, “Characterization of grain boundary disconnections in srtio3 part ii: the influence of superimposed disconnections on image analysis,” *Journal of Materials Science*, vol. 54, pp. 3710–3725, Mar 2019.

[13] M. Hillert, “On the theory of normal and abnormal grain growth,” *Acta Metallurgica*, vol. 13, no. 3, pp. 227–238, 1965.

[14] J. E. Burke and D. Turnbull, “Recrystallization and grain growth,” *Progress in Metal Physics*, vol. 3, pp. 220–292, 1952.

[15] W. Rheinheimer, M. Bäurer, H. Chien, G. S. Rohrer, C. A. Handwerker, J. E. Blendell, and M. J. Hoffmann, “The equilibrium crystal shape of strontium titanate and its relationship to the grain boundary plane distribution,” *Acta Mat.*, vol. 82, pp. 32–40, 2015.

[16] M. Bäurer, H. Kungl, and M. J. Hoffmann, “Influence of sr/ti stoichiometry on the densification behavior of strontium titanate,” *Journal of the American Ceramic Society*, vol. 92, pp. 601–606, 2009.

[17] F. Lemke, W. Rheinheimer, and M. J. Hoffmann, “A comparison of power controlled flash sintering and conventional sintering of strontium titanate,” *Scripta Materialia*, vol. 130, pp. 187–190, 2017.

[18] F. Lemke, W. Rheinheimer, and M. Hoffmann, “Sintering and grain growth in srtio3: impact of defects on kinetics,” *Journal of Ceramic Society of Japan*, vol. 124, no. 4, pp. 346–353, 2016.

[19] W. Rheinheimer, M. Bäurer, C. Handwerker, J. Blendell, and M. Hoffmann, “Growth of single crystalline seeds into polycrystalline strontium titanate: Anisotropy of the mobility, intrinsic drag effects and kinetic shape of grain boundaries,” *Acta Materialia*, vol. 95, pp. 111 – 123, 2015.

[20] B. Nestler, M. Reichardt, and M. Selzer, “Massive multi-phase-field simulations: methods to compute large grain system,” in *Proceedings of the 11th international conference on aluminium alloys*, pp. 1251–1255, 2008.

[21] N. Moelans, B. Blanpain, and P. Wollants, “An introduction to phase-field modeling of microstructure evolution,” *Calphad*, vol. 32, no. 2, pp. 268–294, 2008.

[22] B. Nestler and A. Choudhury, “Phase-field modeling of multi-component systems,” *Current Opinion in Solid State & Materials Science*, vol. 15, no. 3, pp. 93–105, 2011.

[23] B. Nestler, H. Garcke, and B. Stinner, “Multicomponent alloy solidification: Phase-field modeling and simulations,” *Physical Review E*, vol. 71, p. 041609, Apr. 2005.

[24] I. Steinbach, “Phase-field models in materials science,” *Modelling and Simulation in Materials Science and Engineering*, vol. 17, p. 073001, 07 2009.

[25] J. Hötzer, O. Tschukin, M. B. Said, M. Berghoff, M. Jainta, G. Barthelemy, N. Smorchkov, D. Schneider, M. Selzer, and B. Nestler, “Calibration of a multi-phase field model with quantitative angle measurement,” *Journal of Materials Science*, vol. 51, no. 4, pp. 1788–1797, 2016.

[26] I. Steinbach and F. Pezzolla, “A generalized field method for multiphase transformations using interface fields,” *Physica D: Nonlinear Phenomena*, vol. 134, no. 4, pp. 385–393, 1999.

[27] J. Hötzer, A. Reiter, H. Hierl, P. Steinmetz, M. Selzer, and B. Nestler, “The parallel multi-physics phase-field framework pace3d,” *Journal of Computational Science*, vol. 26, pp. 1 – 12, 2018.

[28] S. G. Kim, D. I. Kim, W. T. Kim, and Y. B. Park, “Computer simulations of two-dimensional and three-dimensional ideal grain growth,” *Physical Review E*, vol. 74, no. 6, p. 061605, 2006.

[29] M. Syha and D. Weygand, “A generalized vertex dynamics model for grain growth in three dimensions,” *Modelling and Simulation in Materials Science and Engineering*, vol. 18, p. 015010 (19pp), 2010.

[30] W. Rheinheimer, M. Fülling, and M. J. Hoffmann, “Grain growth in weak electric fields in strontium titanate: Grain growth acceleration by defect redistribution,” *Journal of the European Ceramic Society*, vol. 36, no. 11, pp. 2773 – 2780, 2016.

[31] W. Rheinheimer, J. P. Parras, J.-H. Preusker, R. A. D. Souza, and M. J. Hoffmann, “Grain growth in strontium titanate in electric fields: the impact of space charge on the grain boundary mobility,” *Journal of the American Ceramic Society*, vol. 00, pp. 1–12, 2018.

[32] W. Rheinheimer, X. L. Phuah, H. Wang, F. Lemke, M. J. Hoffmann, and H. Wang, “The role of point defects and defect gradients in flash sintering of perovskite oxides,” *Acta Materialia*, vol. 165, pp. 398 – 408, 2019.

[33] Y.-M. Chiang and T. Takagi, “Grain-boundary chemistry of barium titanate and strontium titanate: I, high-temperature equilibrium space charge,” *Journal of the American Ceramic Society*, vol. 73, no. 11, pp. 3278–3285, 1990.

[34] Y.-M. Chiang and T. Takagi, “Grain-boundary chemistry of barium titanate and strontium titanate: Ii, origin of electrical barriers in positive-temperature-coefficient thermistors,” *Journal of the American Ceramic Society*, vol. 73, pp. 3286–3291, 1990.

[35] J. W. Cahn, “Impurity-drag effect in grain boundary motion,” *Acta Metallurgica*, vol. 10, p. 789, 1962.

[36] R. A. De Souza, “The formation of equilibrium space-charge zones at grain boundaries in the perovskite oxide srtio3,” *Physical Chemistry Chemical Physics*, vol. 11, no. 43, pp. 9939–9969, 2009.

[37] A. R. Kalidindi and C. A. Schuh, “Stability criteria for nanocrystalline alloys,” *Acta Materialia*, vol. 132, pp. 128 – 137, 2017.

[38] R. Kirchheim, “Reducing grain boundary, dislocation line and vacancy formation energies by solute segregation. i. theoretical background,” *Acta Materialia*, vol. 55, no. 15, pp. 5129 – 5138, 2007.

[39] J. Weissmüller, “Alloy effects in nanostructures,” *Nanostructured Materials*, vol. 3, no. 1, pp. 261 – 272, 1993. Proceedings of the First International Conference on Nanostructured Materials.

[40] S. A. Bojarski, M. P. Harmer, and G. S. Rohrer, “Influence of grain boundary energy on the nucleation of complexion transitions,” *Scripta Materialia*, vol. 88, pp. 1–4, Oct. 2014.

[41] S. A. Bojarski, M. Stuer, Z. Zhao, P. Bowen, and G. S. Rohrer, “Influence of y and la additions on grain growth and the grain-boundary character distribution of alumina,” *Journal of the American Ceramic Society*, vol. 97, pp. 622–630, Feb. 2014.

[42] P. R. Cantwell, M. Tang, S. J. Dillon, J. Luo, G. S. Rohrer, and M. P. Harmer, “Grain boundary complexions,” *Acta Materialia*, vol. 62, pp. 1–48, 2014.

[43] M. N. Kelly, S. A. Bojarski, and G. S. Rohrer, “The temperature dependence of the relative grain-boundary energy of yttria-doped alumina,” *Journal of the American Ceramic Society*, vol. 100, no. 2, pp. 783–791, 2017.

[44] G. S. Rohrer, “Grain boundary energy anisotropy: a review,” *Journal of Materials Science*, vol. 46, no. 18, pp. 5881–5895, 2011.

[45] E. A. Holm and S. M. Foiles, “How grain growth stops: A mechanism for grain growth stagnation in pure materials,” *Science*, vol. 328, pp. 1138–1140, 2010.

[46] J. C. Tucker, L. H. Chan, G. S. Rohrer, M. A. Groeber, and A. D. Rollett, “Tail departure of log-normal grain size distributions in synthetic three-dimensional microstructures,” *Metallurgical and Materials Transactions A-physical Metallurgy and Materials Science*, vol. 43A, pp. 2810–2822, Aug. 2012.

[47] M. Upmanyu, G. N. Hassold, A. Kazaryan, E. A. Holm, Y. Wang, B. Patton, and D. J. Srolovitz, “Boundary mobility and energy anisotropy effects on microstructural evolution during grain growth,” *Interface Science*, vol. 10, pp. 201–216, 2002.

[48] W. E. Frazier, G. S. Rohrer, and A. D. Rollett, “Abnormal grain growth in the potts model incorporating grain boundary complexion transitions that increase the mobility of individual boundaries,” *Acta Materialia*, vol. 96, pp. 390–398, Sept. 2015.

[49] A. Kazaryan, Y. Wang, S. A. Dregia, and B. R. Patton, “Grain growth in anisotropic systems: comparison of effects of energy and mobility,” *Acta Materialia*, vol. 50, pp. 2491–2502, June 2002.

[50] Y. Suwa, Y. Saito, and H. Onodera, “Three-dimensional phase field simulation of the effect of anisotropy in grain-boundary mobility on growth kinetics and morphology of grain structure,” *Computational Materials Science*, vol. 40, no. 1, pp. 40–50, 2007.

[51] P. R. Cantwell, S. L. Ma, S. A. Bojarski, G. S. Rohrer, and M. P. Harmer, “Expanding time-temperature-transformation (ttt) diagrams to interfaces: A new approach for grain boundary engineering,” *Acta Materialia*, vol. 106, pp. 78–86, Mar. 2016.

[52] S.-M. Wang and S.-J. L. Kang, “Acceptor segregation and nonlinear current-voltage characteristics in h2-sintered srtio3,” *Applied Physics Letters*, vol. 89, pp. 041910–1 041910–3, 2006.

[53] O. Schumacher, C. J. Marvel, M. N. Kelly, P. R. Cantwell, R. P. Vinci, J. M. Rickman, G. S. Rohrer, and M. P. Harmer, “Complexion time-temperature-transformation (ttt) diagrams: Opportunities and challenges,” *Current Opinion in Solid State and Materials Science*, vol. 20, no. 5, pp. 316 – 323, 2016. Grain boundary complexions -current status and future directions.

Supplementary material

Table S1 lists the experimental conditions for all samples used in this study, i.e. temperatures, heating times, number of grains counted by EBSD for grain size distributions and pixel sizes for the EBSD measurements.

In the following, additional experimental and simulated microstructures are illustrated along with the comparison of the grain size distributions. We are reprinting the figures here to have all data in one row. Each figure displays the data for one temperature at different processing times. In the first column, the measured microstructures are shown. The details are given in the captions. The scale is the same for all microstructures. The color code reflects the orientation of each grain with respect to the sample surface (Fig. S1a). The second column composes the simulated microstructure that was matched with the experiments. The scale of the simulated microstructures is arbitrary and was chosen such that a comparison to the experiments is possible. The color code of the simulated microstructures represents the type of the individual grain (red: fast, blue: slow). The color saturation bases on the relative size of each grain (Fig. S1b and c). Only subsections are presented for both EBSD microstructures and simulated microstructures as the full datasets are too large. In the third column, the measured and simulated grain size distributions are plotted.

As all figures follow the same scheme, a separate discussion is only given if there are features to comment. Considering the following figures, a good match is evident between simulated and measured microstructures. There are a few cases where the match is not optimal. These cases are highlighted here and discussed in the manuscript.

In Fig. S7 g, the match between simulated and measured microstructures is poor for small grain sizes. However, this microstructure is also the most fine-grained one in this study. The pixel size in EBSD was 100 nm, so that the smallest grains are not resolved. For the next two measurements, a smaller pixel size was used (75 nm) and the overall grain size is larger. As such, the resolution problem does not occur.

Fig. S9 f shows the grain size distribution after 5 h at 1460 °C. The measured grain size distribution is very noisy for large grains which is due to insufficient statistics of large grains. The match of simulated and measured microstructures can only be considered qualitatively and the fraction of fast grains found for 1460 °C is uncertain. For 10 h and 20 h heating time, the statistics are even worse (Fig. S10 c) and no match between experiments and simulations could be found for these cases. Similar issues appear at 1480 °C (Fig. 5 n and o) and at 1500 °C (Fig. S11 i and Fig. S12 b).

Table S1 List of heating times, number of grains contained in the respective EBSD measurement and pixel size for each EBSD measurement.

T [°C]	**Heating times [h]**					**Number of grains [-]**					**Pixel size [nm]**				
1350	1	5	10			3857	5799	3058			76	93	120		
1360	1	5	10			13305	5191	5031			119	111	119		
1370	1	5	10			7485	4968	4964			89	134	186		
1380	2	5	10			14178	5794	3877			107	107	120		
1390	2	5	10			7665	6522	2537			75	84	93		
1400	2	5	10			13780	7845	5236			93	93	93		
1410	2	5	10			14499	13269	7918			75	93	93		
1425	2	5	10			37640	17365	9628			100	77	75		
1440	1	3	8	18		11739	5567	11849	7750		93	93	120	93	
1460	1,5	5	10	20		11196	4458	1070	1092		93	120	120	150	
1480	0,1	0,2	0,5	1	2	13600	12808	5267	5966	1898	93	120	129	120	120
1500	0,1	0,5	1,5	3,5		13513	11616	4147	1357		100	134	172	120	

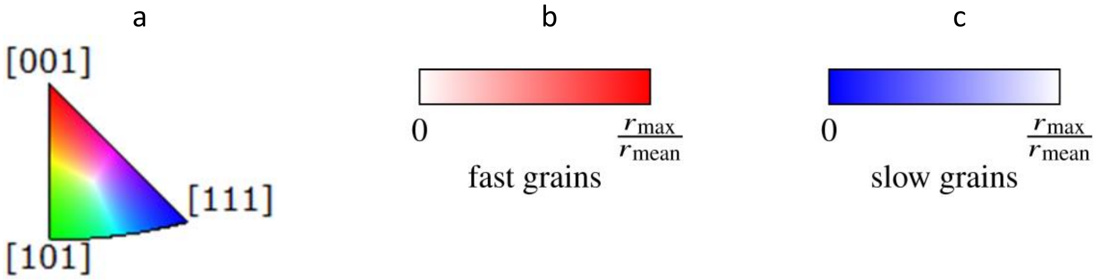

Fig. S1 Orientation legend for all EBSD datasets (a) and color code for the fast (red, b) and slow grains (blue, c). The saturation bases on the relative size of individual grains.

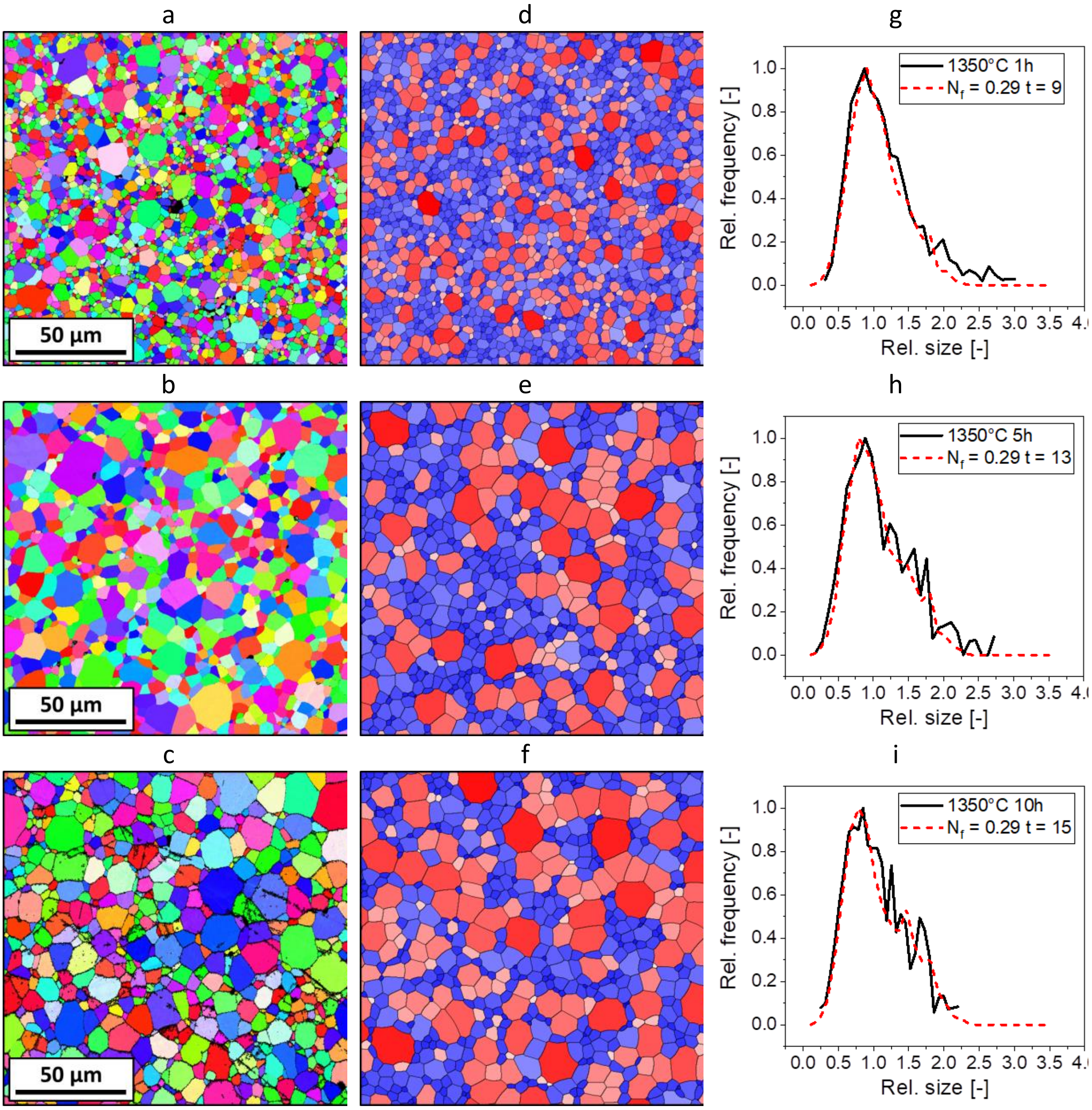

Fig. S2 Microstructure evolution at 1350 °C. EBSD images of the microstructures after 1 h (a), 5 h (b) and 10 h (c). d-f simulated microstructures corresponding to a-c. The fraction of fast grains was 0.29. g-i comparison of measured and simulated grain size distributions. The color in a-c gives the surface orientation of the grains according to the legend in Fig. S1 a. In d-f, the color refers to the relative mobility of the respective grain (blue: slow, red: fast). The saturation illustrates the individual grain size according to the legends in Fig. S1 b and c.

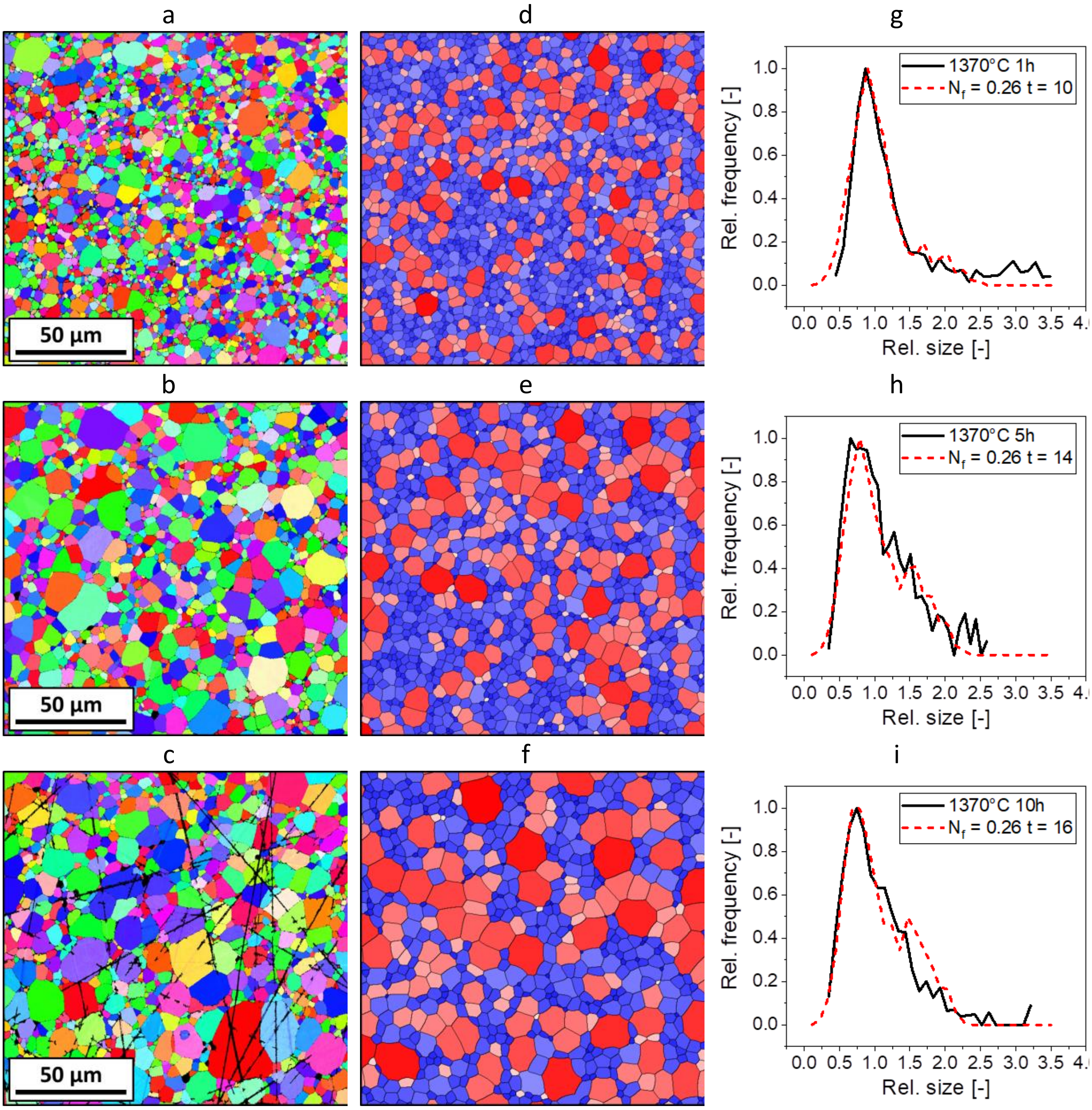

Fig. S3 Microstructure evolution at 1370 °C. EBSD images of the microstructures after 1 h (a), 5 h (b) and 10h (c). d-f simulated microstructures corresponding to a-c. The fraction of fast grains was 0.26. g-i comparison of measured and simulated grain size distributions.

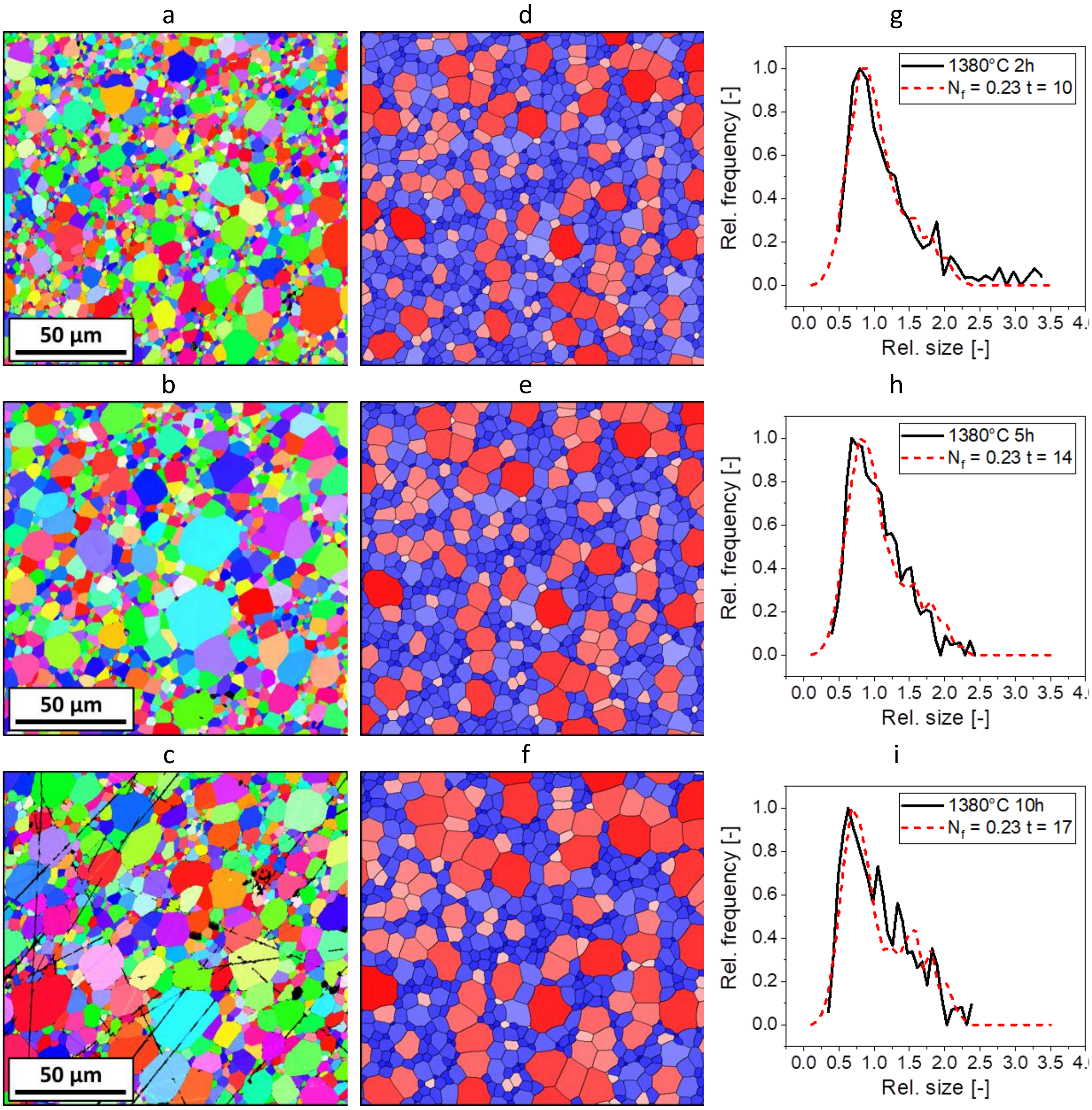

Fig. S4 Microstructure evolution at 1380 °C. EBSD images of the microstructures after 2 h (a), 5 h (b) and 10 h (c). d-f simulated microstructures corresponding to a-c. The fraction of fast grains was 0.23. g-i comparison of measured and simulated grain size distributions.

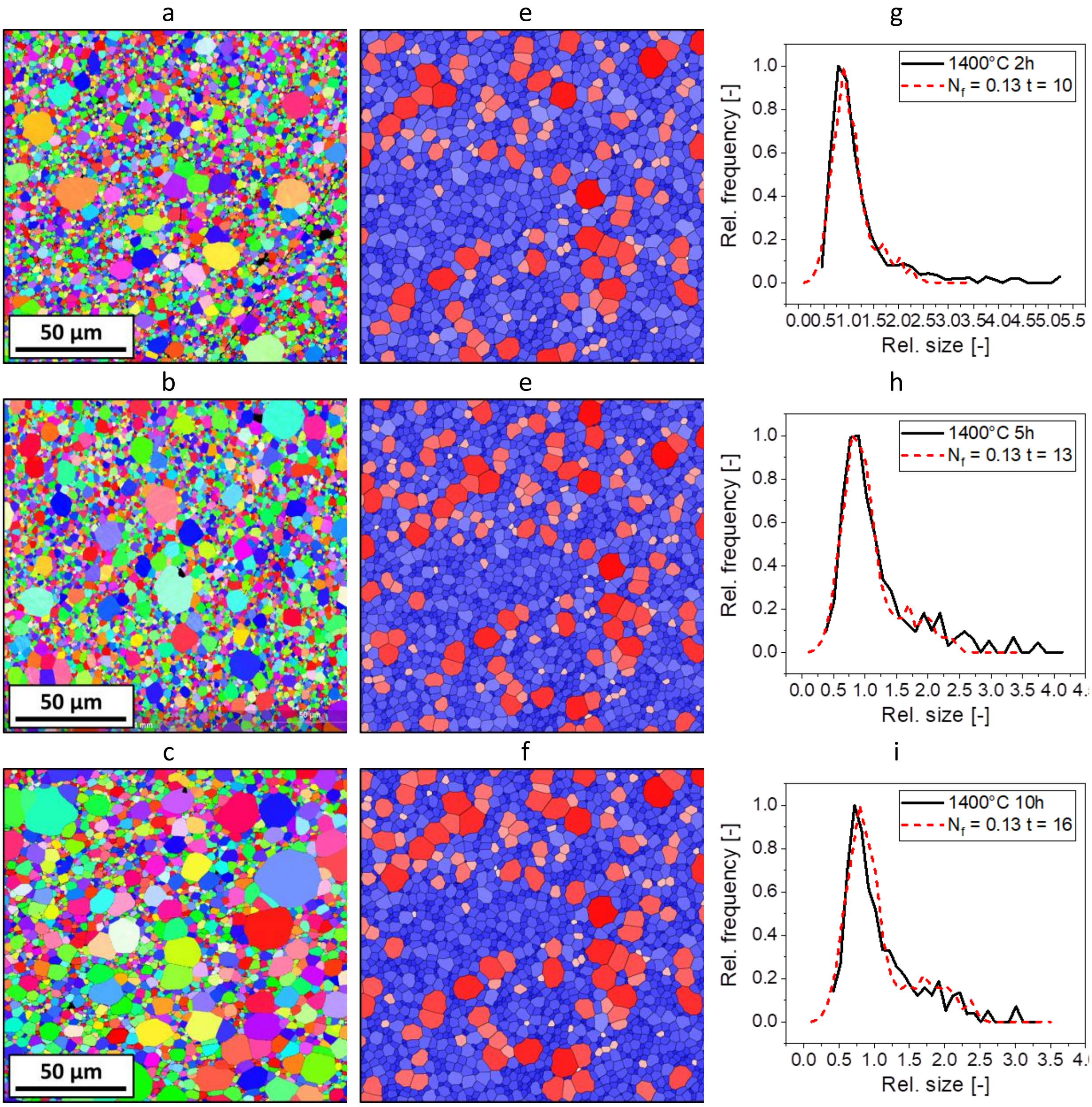

Fig. S5 Microstructure evolution at 1400 °C. EBSD images of the microstructures after 2 h (a), 5 h (b) and 10 h (c). d-f simulated microstructures corresponding to a-c. The fraction of fast grains was 0.13. g-i comparison of measured and simulated grain size distributions.

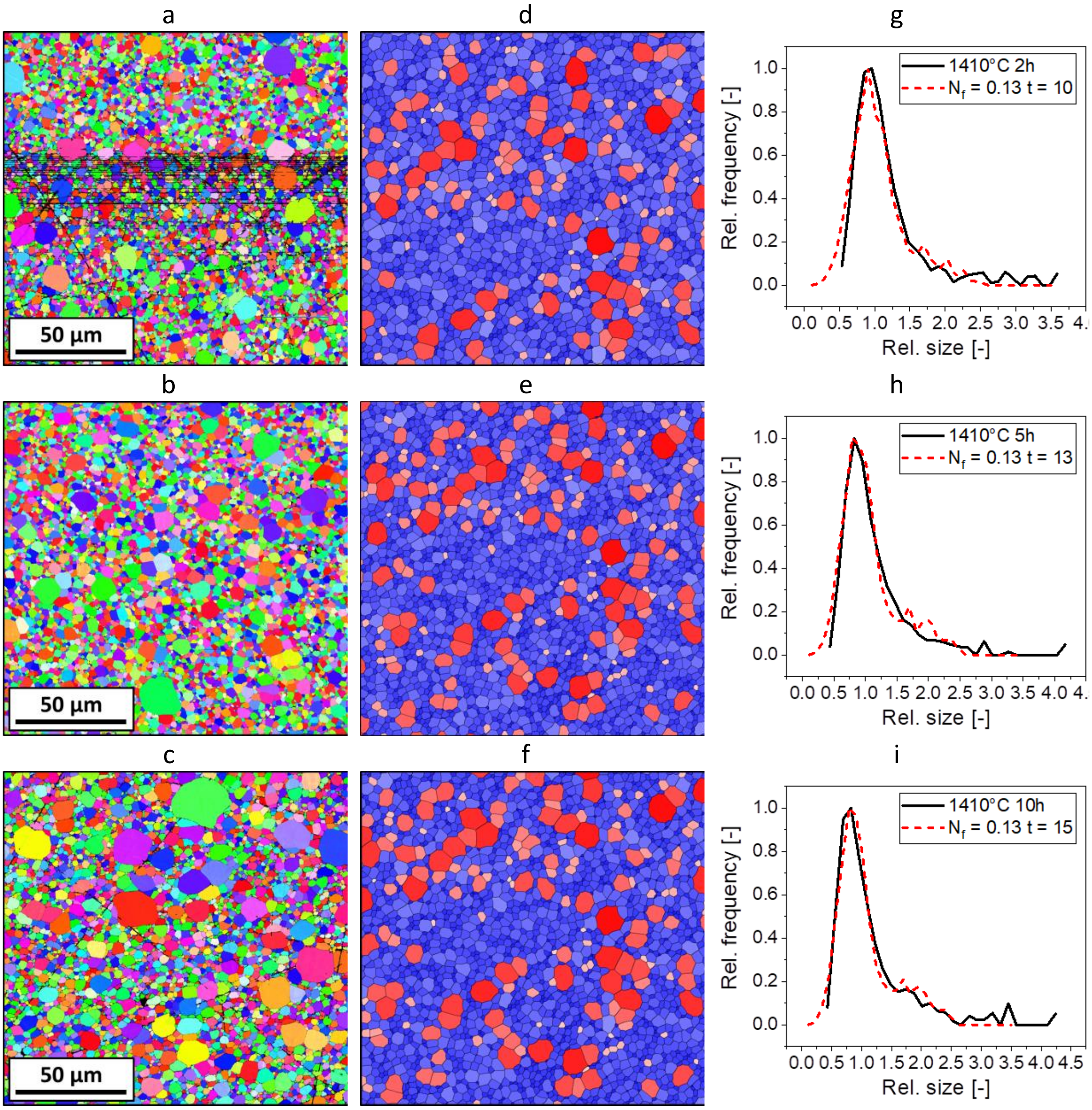

Fig. S6 Microstructure evolution at 1410 °C. EBSD images of the microstructures after 2 h (a), 5 h (b) and 10 h (c). d-f simulated microstructures corresponding to a-c. The fraction of fast grains was 0.13. g-i comparison of measured and simulated grain size distributions.

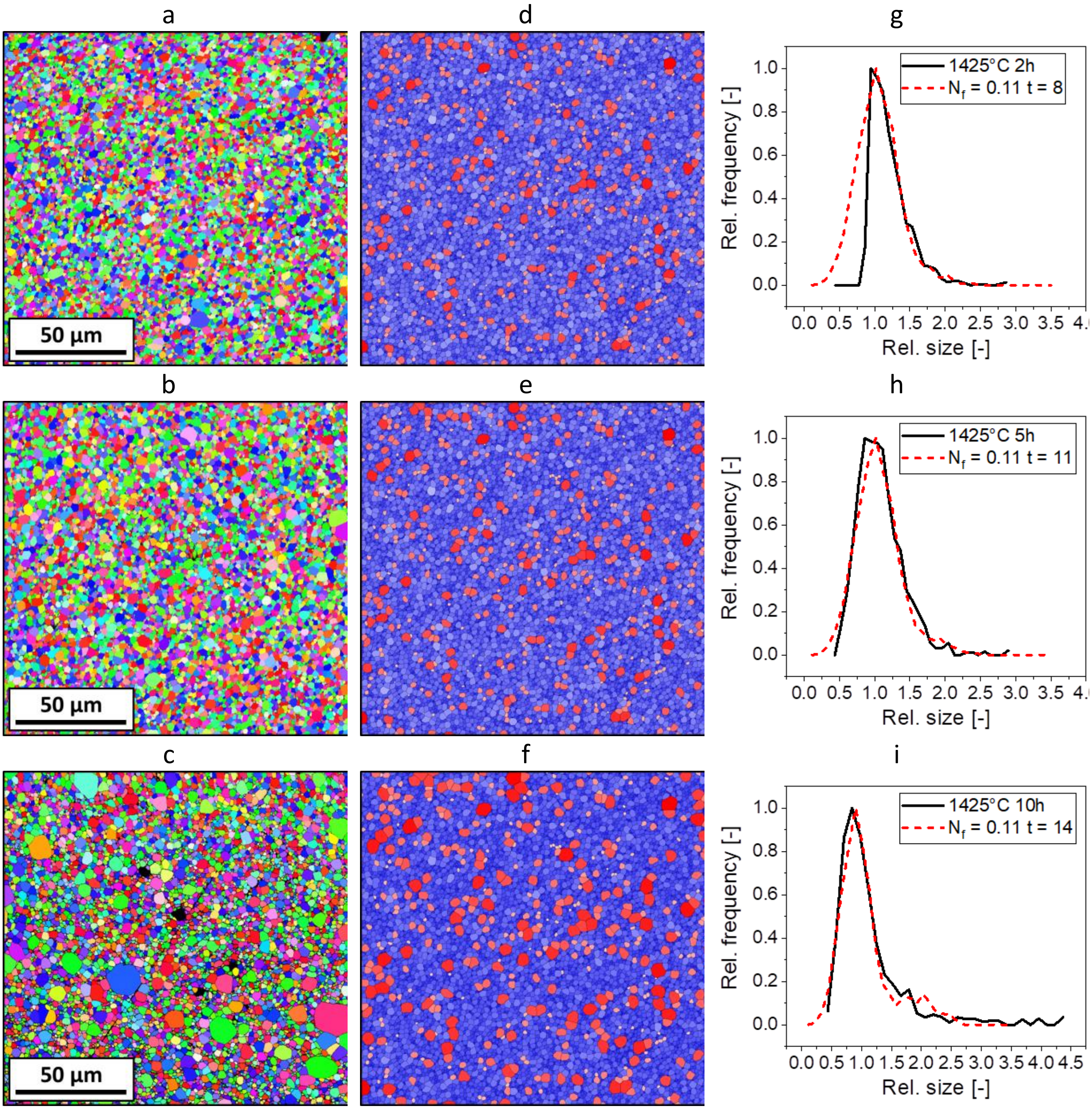

Fig. S7 Microstructure evolution at 1425 °C. EBSD images of the microstructures after 2 h (a), 5 h (b) and 10 h (c). d-f simulated microstructures corresponding to a-c. The fraction of fast grains was 0.11. g-i comparison of measured and simulated grain size distributions.

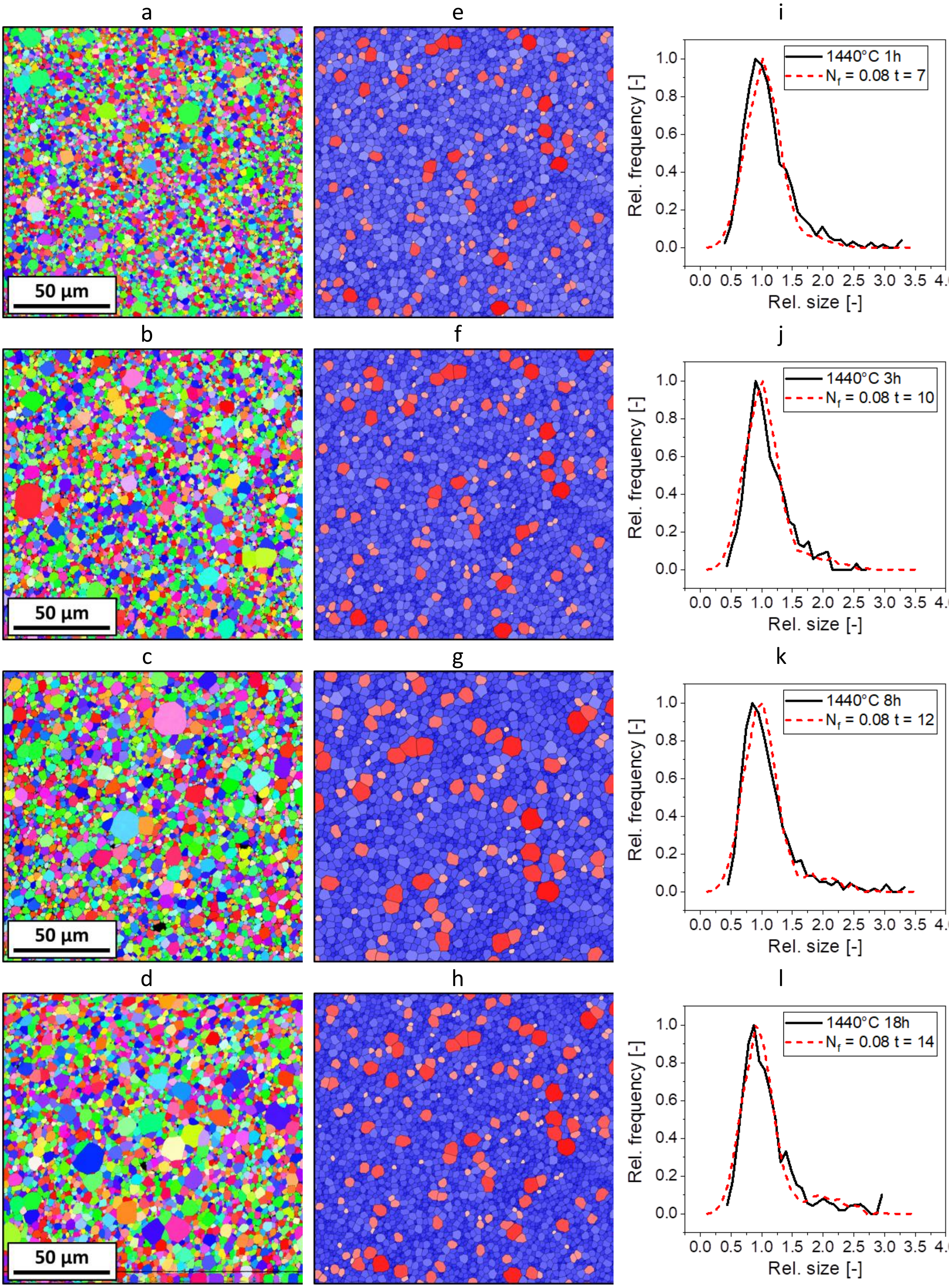

Fig. S8 Microstructure evolution at 1440 °C. EBSD images of the microstructures after 1 h (a), 3 h (b), 8 h (c) and 18 h (d). e-h simulated microstructures corresponding to a-d. The fraction of fast grains was 0.08. i-l comparison of measured and simulated grain size distributions.

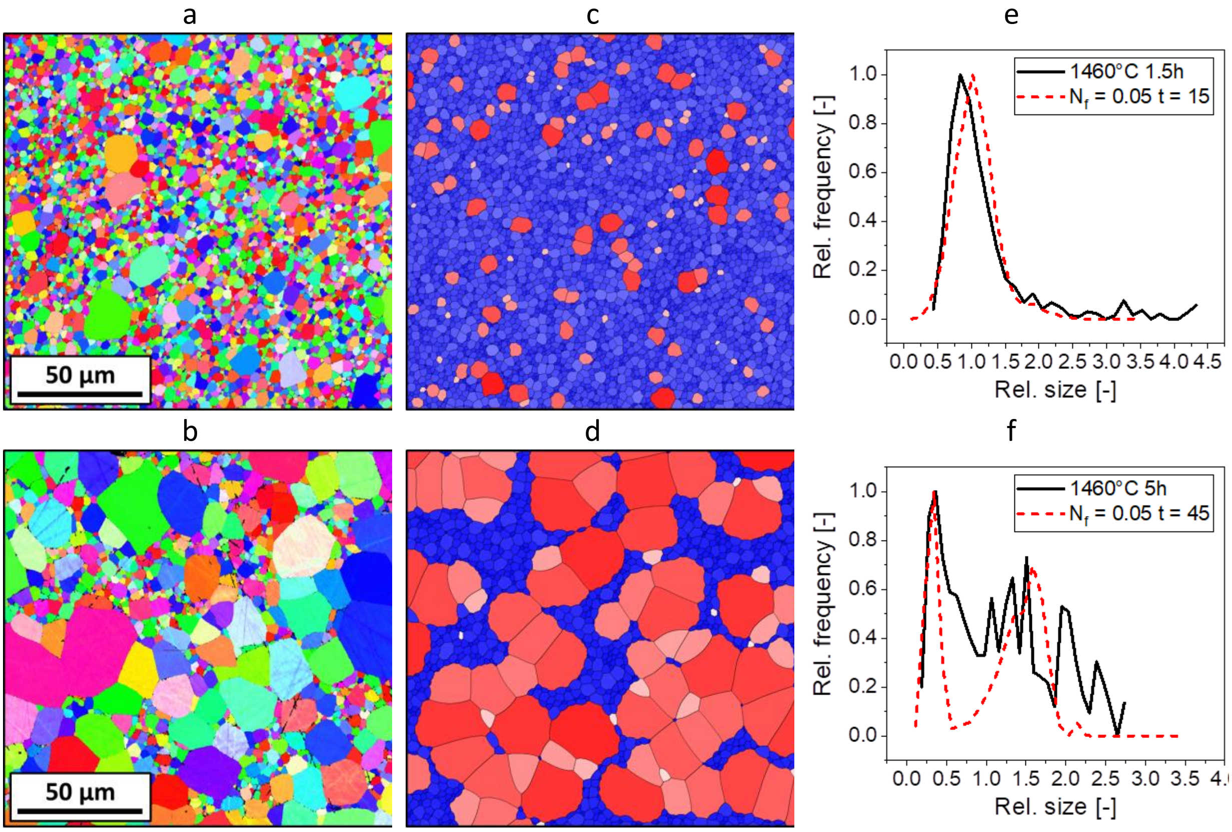

Fig. S9 Microstructure evolution at 1460 °C. EBSD images of the microstructures after 2 h (a) and 5 h (b).c and d simulated microstructures corresponding to a and b. The fraction of fast grains was 0.05. e and f comparison of measured and simulated grain size distributions.

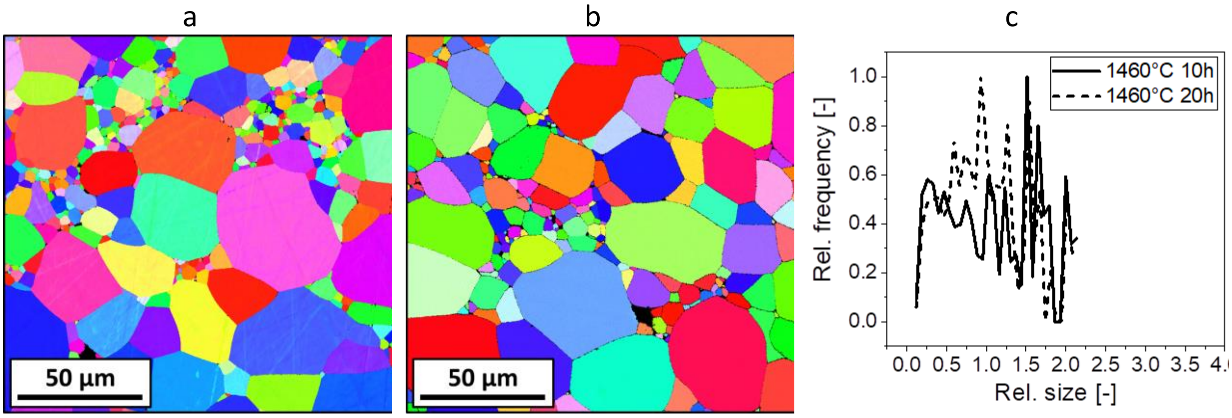

Fig. S10 Microstructure evolution at 1460 °C. EBSD images of the microstructures after 10 h (a) and 20 h (b) and corresponding grain size distributions (c). Due to the insufficient statistics for large grains, the grain size distribution contains significant scattering. A comparison to simulated grain size distributions was not possible.

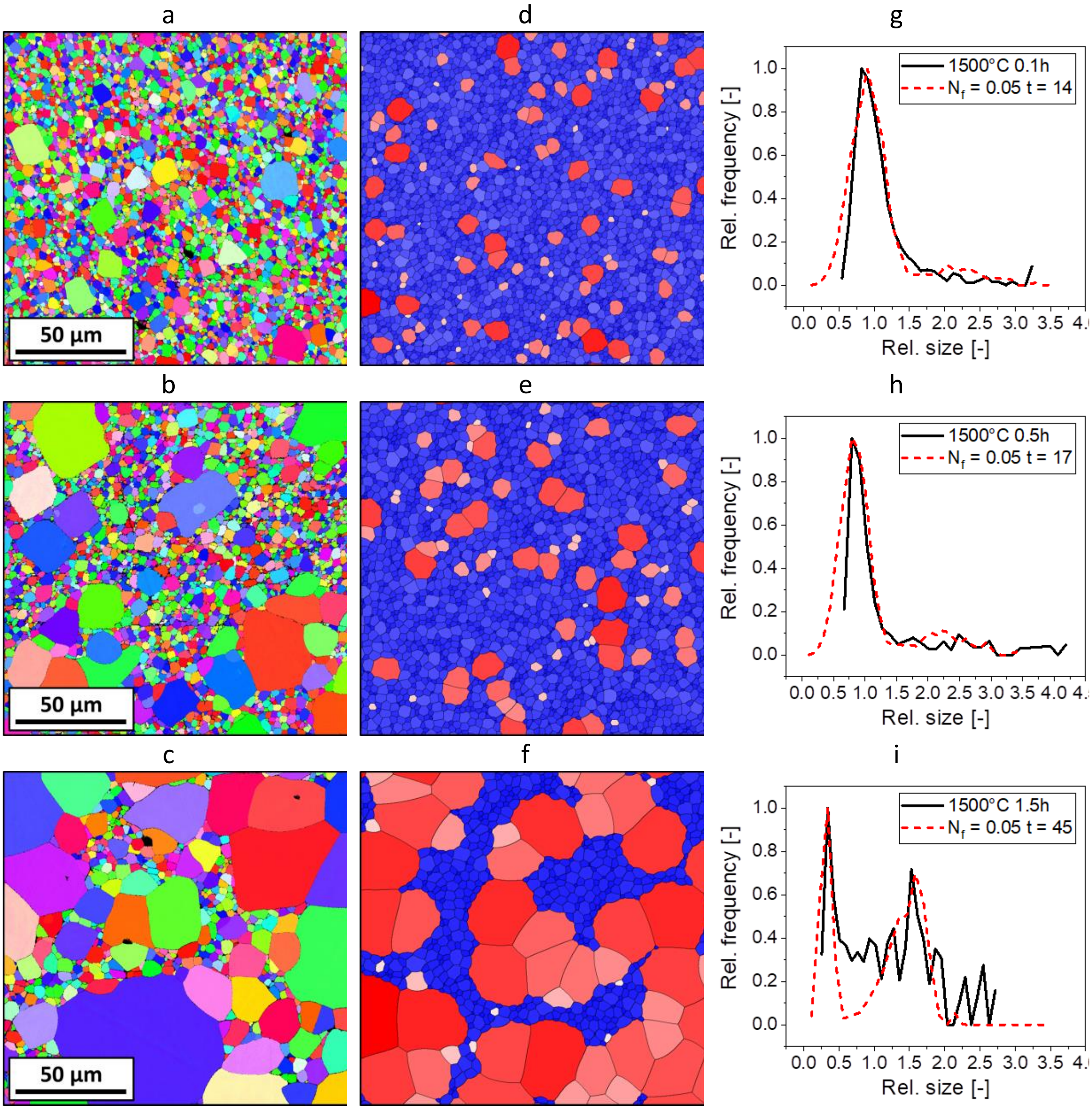

Fig. S11 Microstructure evolution at 1500 °C. EBSD images of the microstructures after 0.1 h (a), 0.5 h (b) and 1.5 h (c). d-f simulated microstructures corresponding to a-c. The fraction of fast grains was 0.05. g-i comparison of measured and simulated grain size distributions.

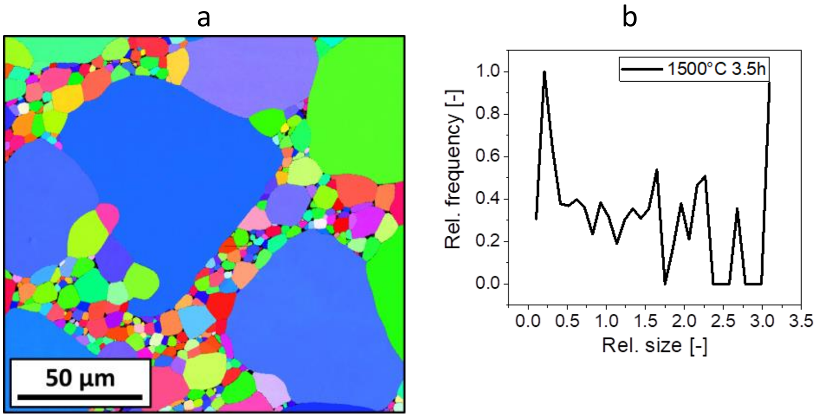

Fig. S12 Microstructure after 3.5 h at 1500°C (a) and corresponding grain size distribution (b). Due to insufficient statistics of large grains, a comparison to simulation data was not possible.